SN 2010jl: OPTICAL TO HARD X-RAY OBSERVATIONS REVEAL AN EXPLOSION EMBEDDED IN A TEN SOLAR MASS COCOON

ERAN O. OFEK[1], ANDREAS ZOGLAUER[2], STEVEN E. BOGGS[2], NICOLAS M. BARRIÉRE[2], STEPHEN P. REYNOLDS[3], CHRIS L. FRYER[4],
FIONA A. HARRISON[5], S. BRADLEY CENKO[6,7], SHRINIVAS R. KULKARNI[5], AVISHAY GAL-YAM[1], IAIR ARCAVI[1], ERIC BELLM[5],
JOSHUA S. BLOOM[6], FINN CHRISTENSEN[8], WILLIAM W. CRAIG[9], WESLEY EVEN[4], ALEXEI V. FILIPPENKO[6], BRIAN GREFENSTETTE[5],
CHARLES J. HAILEY[9], RUSS LAHER[10], KRISTIN MADSEN[5], EHUD NAKAR[11], PETER E. NUGENT[12], DANIEL STERN[13],
MARK SULLIVAN[14], JASON SURACE[10], AND WILLIAM W. ZHANG[7]

[1] Benoziyo Center for Astrophysics, Weizmann Institute of Science, 76100 Rehovot, Israel
[2] Space Sciences Laboratory, Department of Physics, University of California, 7 Gauss Way, Berkeley, CA 94720, USA
[3] Department of Physics, North Carolina State University, Raleigh, NC 27695-8202, USA
[4] CCS Division, Los Alamos National Laboratory, Los Alamos, NM 87545, USA
[5] Cahill Center for Astronomy and Astrophysics, California Institute of Technology, Pasadena, CA 91125, USA
[6] Department of Astronomy, University of California, Berkeley, CA 94720-3411, USA
[7] Astrophysics Science Division, NASA Goddard Space Flight Center, Mail Code 661, Greenbelt, MD 20771, USA
[8] DTU Space-National Space Institute, Technical University of Denmark, Elektrovej 327, DK-2800 Lyngby, Denmark
[9] Columbia Astrophysics Laboratory, 538 West 120th Street, New York, NY 10027, USA
[10] Spitzer Science Center, MS 314-6, California Institute of Technology, Pasadena, CA 91125, USA
[11] Raymond and Beverly Sackler School of Physics and Astronomy, Tel Aviv University, Tel Aviv 69978, Israel
[12] Computational Cosmology Center, Lawrence Berkeley National Laboratory, 1 Cyclotron Road, Berkeley, CA 94720, USA
[13] Jet Propulsion Laboratory, California Institute of Technology, Pasadena, CA 91109, USA
[14] School of Physics and Astronomy, University of Southampton, Southampton SO17 1BJ, UK

ABSTRACT

Some supernovae (SNe) may be powered by the interaction of the SN ejecta with a large amount of circumstellar matter (CSM). However, quantitative estimates of the CSM mass around such SNe are missing when the CSM material is optically thick. Specifically, current estimators are sensitive to uncertainties regarding the CSM density profile and the ejecta velocity. Here we outline a method to measure the mass of the optically thick CSM around such SNe. We present new visible-light and X-ray observations of SN 2010jl (PTF 10aaxf), including the first detection of an SN in the hard X-ray band using *NuSTAR*. The total radiated luminosity of SN 2010jl is extreme—at least 9×10^{50} erg. By modeling the visible-light data, we robustly show that the mass of the circumstellar material within $\sim 10^{16}$ cm of the progenitor of SN 2010jl was in excess of $10\,M_\odot$. This mass was likely ejected tens of years prior to the SN explosion. Our modeling suggests that the shock velocity during shock breakout was ~ 6000 km s^{-1}, decelerating to ~ 2600 km s^{-1} about 2 yr after maximum light. Furthermore, our late-time *NuSTAR* and *XMM* spectra of the SN presumably provide the first direct measurement of SN shock velocity 2 yr after the SN maximum light—measured to be in the range of 2000–4500 km s^{-1} if the ions and electrons are in equilibrium, and $\gtrsim 2000$ km s^{-1} if they are not in equilibrium. This measurement is in agreement with the shock velocity predicted by our modeling of the visible-light data. Our observations also show that the average radial density distribution of the CSM roughly follows an r^{-2} law. A possible explanation for the $\gtrsim 10\,M_\odot$ of CSM and the wind-like profile is that they are the result of multiple pulsational pair instability events prior to the SN explosion, separated from each other by years.

Key words: stars: mass-loss – supernovae: general – supernovae: individual (SN 2010jl)

Online-only material: color figures, machine-readable tables

1. INTRODUCTION

Some supernovae (SNe), especially of Type IIn (for a review, see Filippenko 1997), show strong evidence for the existence of a large amount (i.e., $\gtrsim 10^{-3}\,M_\odot$) of circumstellar matter (CSM) ejected months to years prior to the SN explosion (e.g., Dopita et al. 1984; Weiler et al. 1991; Chugai & Danziger 1994; Chugai et al. 2003; Gal-Yam et al. 2007; Gal-Yam & Leonard 2009; Ofek et al. 2007, 2010, 2013b; Smith et al. 2007, 2008, 2009; Kiewe et al. 2012). In some cases even larger CSM masses, of order $10\,M_\odot$, have been reported. However, these claims are based on very rough modeling that may suffer from more than an order of magnitude uncertainty (e.g., see Moriya & Tominaga 2012 for discussion). Interestingly, five SNe were recently reported to show outbursts taking place prior to the SN explosion (e.g., Pastorello et al. 2007, 2013; Foley et al. 2007,

2011; Mauerhan et al. 2013; Corsi et al. 2013; Fraser et al. 2013; Ofek et al. 2013b).

Interaction of the SN blast wave with the CSM in many cases produces long-lived panchromatic signals from radio to X-ray energies (e.g., Slysh 1990; Chevalier & Fransson 1994; Chevalier 1998; Weiler et al. 1991; Chandra et al. 2012a, 2012b; Ofek et al. 2013a). Most important for the interpretation of the light curves of some SNe IIn, Svirski et al. (2012) have presented predictions for the optical and X-ray luminosity evolution of SNe powered by interaction of their ejecta with the CSM. Observing these signals has the potential to both unveil the physical parameters of the explosion and measure the CSM mass.

Until recently, hard X-ray instruments lacked the sensitivity to study SN shock interactions. However, with the launch of the *Nuclear Spectroscopic Telescope Array* (*NuSTAR*) focusing

hard X-ray space telescope (Harrison et al. 2013), it is now possible to measure the hard X-ray spectrum (3–79 keV) of such events. This in turn has the potential to directly measure, in some cases, the shock velocity of the SN, which is hard to estimate using other proxies. Here we present the first detection of an SN (SN 2010jl, also known as PTF 10aaxf) outside the Local Group in the hard X-ray band using *NuSTAR*.

SN 2010jl was discovered on 2010 November 3.5 (Newton & Puckett 2010) in the star-forming galaxy UGC 5189A (redshift $z = 0.0107$, distance 49 Mpc) and was classified as an SN IIn (Benetti et al. 2010; Yamanaka et al. 2010). The SN coordinates, as measured in images taken by the Palomar Transient Factory, are $\alpha = 09^h42^m53^s.337$, $\delta = +09°29'42''.13$ (J2000.0). Pre-discovery images suggest that the SN exploded prior to 2010 October 10 (Stoll et al. 2011). However, the rise time and explosion date are not well constrained. Based on analysis of archival *Hubble Space Telescope* images, Smith et al. (2010) argued that the progenitor mass is $\gtrsim 30 M_\odot$. Stoll et al. (2011) show that the SN host galaxy has a metallicity of $\lesssim 0.3$ solar.

Zhang et al. (2012) reported on photometric and spectroscopic observations of SN 2010jl for the first 1.5 yr after its discovery. They reported that the Hα luminosities of this SN are among the highest ever observed for any SN. Based on a simple CSM-interaction model (i.e., conversion of kinetic energy to luminosity), they estimate that the progenitor lost an order of 30–50 $M_\odot$ a few decades prior to explosion.

Patat et al. (2011) report on spectropolarimetry of SN 2010jl obtained about 15 days after its discovery. They find a significant, and almost constant with wavelength, linear polarization level (1.7%–2.0%) with constant position angle. Based on that, they suggest that the axial ratio of the photosphere of the event is $\lesssim 0.7$. They also note that the Balmer-line cores have small polarization, indicating that they form above the photosphere. They also argue that at the epoch of their observations, the CSM had a very low dust content.

Soon after its discovery, SN 2010jl was detected in X-rays (Chandra et al. 2012a; Ofek et al. 2013a). Chandra et al. (2012a) analyzed the first two *Chandra* observations of this source. They find a high bound-free absorption column density, roughly 10^{24} cm^{-2}, about one month after SN maximum light, decreasing to $\sim 3 \times 10^{23}$ cm^{-2} about 1 yr after maximum light. However, the value of the column density depends on the assumed emission model. Chandra et al. (2012a) reported that the hardest X-ray component in the SN 2010jl spectra has a temperature above 8 keV, but given the *Chandra* drop in sensitivity above 8 keV, this temperature is not well constrained. Here we also reanalyze the *Chandra* observations. Based on the X-ray observations of SN 2010jl, Ofek et al. (2013a) suggested that the optical luminosity of this SN is powered by shock breakout in an optically thick CSM.

Here we analyze *NuSTAR*, *XMM-Newton*, *Chandra*, and *Swift*-XRT as well as visible-light and ultraviolet (UV) observations of the extraordinary Type IIn SN 2010jl. Under the conditions we show to hold for it, at early times after explosion the shock in the dense wind is radiation dominated. That is, the energy density behind the shock is primarily in radiation because of the high Thomson optical depths. In this case, the shock breaks out (i.e., is detectable to a distant observer) when the photon diffusion time is comparable to the dynamical time. Straightforward considerations relate the shock radius, velocity, mass in the wind ahead of the shock, and luminosity, so that the CSM mass can be inferred. We generalize earlier discussions to different power-law profiles for the wind and the SN ejecta to

Table 1
Photometric Observations

Telescope	Filter	MJD− 55,474 (day)	Mag (mag)	Err (mag)
PTF	R	−178.762	<21.8	. . .
PTF	R	39.444	13.514	0.003
PTF	R	39.487	13.519	0.002
PTF	R	40.489	13.532	0.004
PTF	R	40.533	13.532	0.004

Notes. PTF, ASAS (Stoll et al. 2011), and *Swift*-UVOT photometric observations of SN 2010jl. Time is measured relative to MJD 55,474 (20 days prior to the *I*-band peak magnitude). The PTF and *Swift* magnitudes are given in the AB system, while the ASAS measurements are in the Vega system.

(This table is available in its entirety in a machine-readable form in the online journal. A portion is shown here for guidance regarding its form and content.)

obtain general relations among these quantities, and we apply them to optical and X-ray observations of SN 2010jl. Combining our model with the observations, we are able to measure the total CSM mass, its density profile, and the temporal evolution of the shock velocity.

We note that throughout the paper dates are given in the Coordinated Universal Time system, and unless specified differently, errors represent the 1σ uncertainties. The structure of this paper is as follows. We present the observations in Section 2, and the reduction of the X-ray data is discussed in Section 3. Our model is described in Section 4. In Section 5 we apply the model to the observations, and we discuss our results in Section 6.

2. OBSERVATIONS

We obtained multi-wavelength observations of SN 2010jl. The most constraining observations for our model are the bolometric light curve of the SN and the late-time X-ray spectrum obtained by *NuSTAR* + *XMM*. We note that the bolometric light curve is derived from the *R*-band observations with a bolometric correction that we estimate from the *Swift*-UVOT and spectroscopic observations.

2.1. Visible-light Observations

The Palomar Transient Factory (PTF[15]; Law et al. 2009; Rau et al. 2009) detected SN 2010jl (PTF 10aaxf) on 2010 November 13.4, 10 days after its discovery by Newton & Puckett (2010). The PTF data-reduction pipeline is presented by R. Laher et al. (in preparation), and the photometric calibration is described by Ofek et al. (2012a, 2012b). The PTF light curve of this SN and the All Sky Automated Survey (ASAS) prediscovery data points from Stoll et al. (2011) are presented in Figure 1 and listed in Table 1. ASAS first detected the SN on 2010 September 10, about 15 days prior to *I*-band maximum light—soon after its solar conjunction.

The first-year PTF flux measurements taken before MJD 55,760 show a clear power-law decline (Section 5); the second-year flux measurements obtained between MJD 55760 and MJD 56,070 (Figure 1) are consistent with an exponential decay (i.e., $\propto \exp(-t/\tau_{exp})$, where t is the time and τ_{exp} is the exponential timescale). We find that the best-fit exponential timescale is $\tau_{exp} = 129.8 \pm 1.5$ day (χ^2/dof $= 0.7/15$), where
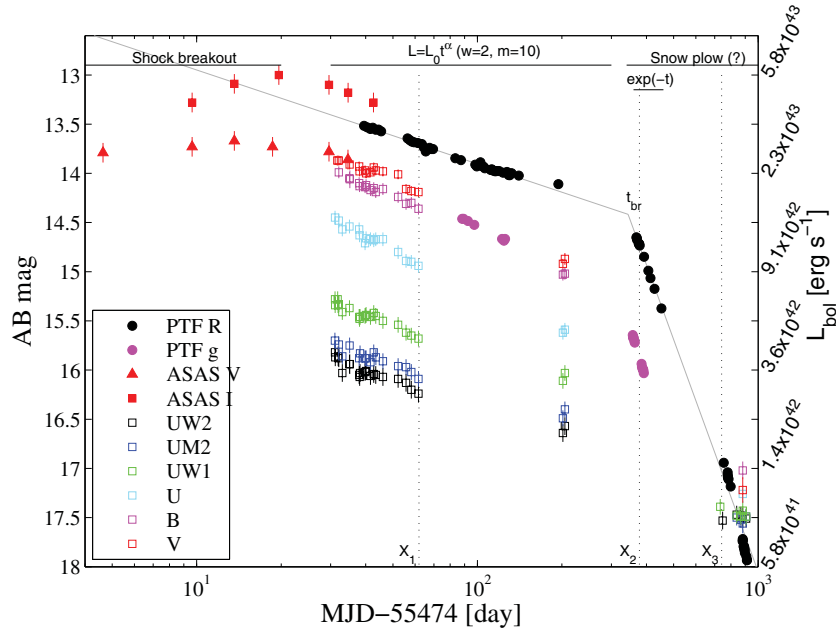
---

[15] http://www.astro.caltech.edu/ptf/

Figure 1. Optical light curves of SN 2010jl. The black filled circles and magenta filled circles represent the PTF measurements, which are based on image subtraction. In this case the uncertainties include the Poisson error and a 0.015 mag systematic error added in quadrature (Ofek et al. 2012a, 2012b). See the legend for ASAS and *Swift*-UVOT measurements. The gray lines show the best-fit broken power law to the PTF *R*-band data. The power-law index before (after) the break is -0.38 (-3.14). The power-law break is at day 344 (with respect to MJD 55,474). The epochs of the *Chandra* and *NuSTAR* + *XMM* observations are marked by vertical dotted lines. The right-hand ordinate axis shows the bolometric luminosity for the PTF *R*-band data, assuming that the bolometric correction is -0.27 mag. Time is measured from 20 days prior to *I*-band maximum light. The various physical stages are indicated at the top of the plot. These are the shock-breakout phase, the early power-law decay, and the snow-plow phase (see Section 4). Also shown is the section of the light curve that is fitted well by an exponential decay (i.e., "exp($-t$)").

the uncertainty is estimated using the bootstrap technique (Efron 1982; Efron & Tibshirani 1993). We note that this is longer than the timescale expected from ^{56}Co decay ($\sim$111 day). Were this decay produced by ^{56}Ni decay to ^{56}Co and finally ^{56}Fe, then at least 27 $M_\odot$ of ^{56}Ni would be required, which is unlikely. Moreover, at later times the decay rate becomes significantly slower than the exponential decay expected from radioactive material (see Figure 1). Therefore, a more reasonable interpretation is that the SN light curve is powered by interaction of the SN shock with CSM. Interestingly, the second-year and third-year data (MJD $>$56,070) are also roughly consistent with a power-law decay. The power-law fits to the light-curve data are shown in Figure 1 and discussed in Section 5.

Zhang et al. (2012) reported on a flattening in the optical light curve of the SN, starting about 90 days after maximum light. However, this flattening is somewhat larger than we measure in the PTF *R*-band data (A possible theoretical explanation for the flattening is discussed in Section 5.1). We note that Zhang et al. (2012) did not use image subtraction, due to the lack of a reference image, and instead they subtracted an estimate of the host light obtained from the Sloan Digital Sky Survey (SDSS) image. According to the SDSS source catalog, the magnitude of the underlying host galaxy is $r \cong 15.5$, which is about 30% of the SN flux at about 200 days after maximum light. This may be large enough to contaminate their photometry. Given that the inconsistency is small ($\sim$0.05 mag), we speculate that the late-time flattening reported by Zhang et al. (2012) is due to contamination from the host galaxy.

2.2. Spectroscopy

SN 2010jl was observed spectroscopically by the PTF collaboration on several occasions. A log file of the observations is presented in Table 2. The data will be electronically released

Table 2
Visible-light Spectroscopic Observations

MJD (day)	Day (day)	Telescope	Instrument	T_{eff} (K)
55,505	31	Keck	LRIS	7560
55,507	33	Keck	DEIMOS	6800
55,507	33	Keck	DEIMOS	6320
55,515	41	Lick	Kast	7090
55,530	56	Lick	Kast	7360
55,538	64	Keck	LRIS	7160
55,565	91	Lick	Kast	6590
55,587	113	Lick	Kast	6650
55,594	120	Lick	Kast	6740
55,864	390	P200	DBSP	6380
56,332	858	Keck	LRIS	10,400
56,414	940	P200	DBSP	10,600
56,421	947	Keck	LRIS	11,670
56,452	978	Keck	LRIS	9350

Notes. MJD is the modified Julian day. Day is the time relative to MJD 55,474 (i.e., 20 days before the *I*-band peak flux). The formal uncertainties in the temperature measurements are about 50–300 K. However, due to metal-line blanketing, the actual effective temperature can be higher. A large fraction of the spectroscopic observations listed here were presented and discussed in Smith et al. (2012).

via the WISeREP Web site[16] (Yaron & Gal-Yam 2012). Selected spectra of SN 2010jl are shown in Figure 2.

Inspection of the spectra of SN 2010jl shows that the Hα line consists of several components. The narrowest features we detected are Hα, Hβ, and He I P Cygni lines, with a velocity difference between the peak and minimum of $\sim$70 km s^{-1}

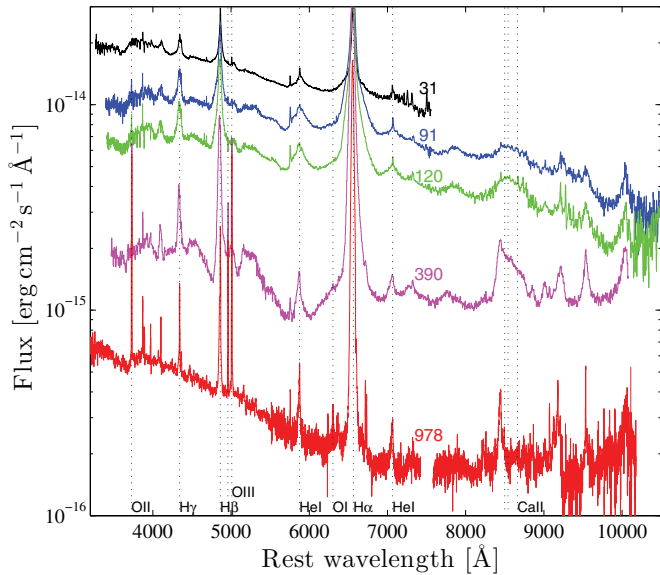[16] http://www.weizmann.ac.il/astrophysics/wiserep/

3

Figure 2. Selected visible-light spectra of SN 2010jl. The number near each spectrum marks its age in days (see Table 2). The last spectrum taken on day 978 may be contaminated by emission from the underlying star-forming region.
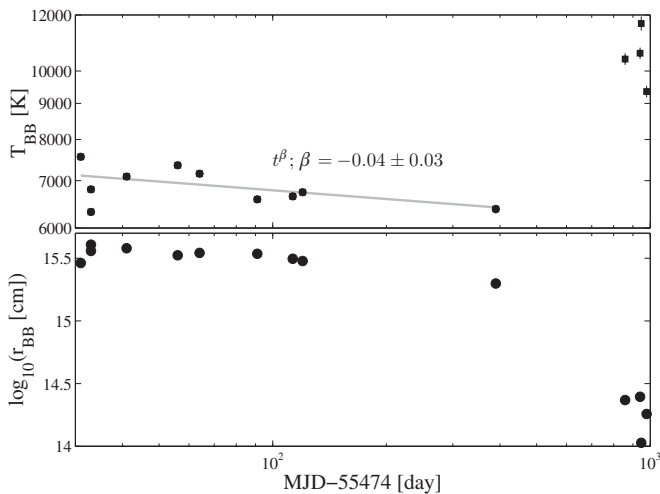(A color version of this figure is available in the online journal.)

Figure 3. Temperature and radius of a blackbody that best fits the visible-light spectroscopic observations as a function of time. Before fitting the spectra, we corrected the flux normalization by comparing the spectra synthetic photometry with the PTF R-band magnitudes. We also removed the prominent emission lines and the Balmer discontinuity. We note that because of additional metal-line blanketing, this estimate is likely a lower limit on the actual temperature. The gray line shows the best-fit power law to the temperature measurements in the first 390 days. The measurements marked by squares were obtained clearly after the break in the optical light curve and were not used in the fit of the temperature as a function of time. These late-time measurements may be contaminated by the host-galaxy light.

(see also Smith et al. 2012). The Hα profile in the spectra can be decomposed into a Lorentzian and a Gaussian, where the Gaussian has a velocity width of $\sigma \approx 300$ km s^{-1}. Alternatively, the early-time spectra can be decomposed into three Gaussians, in which the widest Gaussian has velocity width $\sigma \approx 4000$ km s^{-1}. At late times, about six months after maximum light, the Hα line develops some asymmetry; it is discussed by Smith et al. (2012) and attributed to dust formation. We fitted a blackbody spectrum to the spectroscopic measurements as a function of time, and the derived blackbody temperatures and radii are shown in Figure 3.
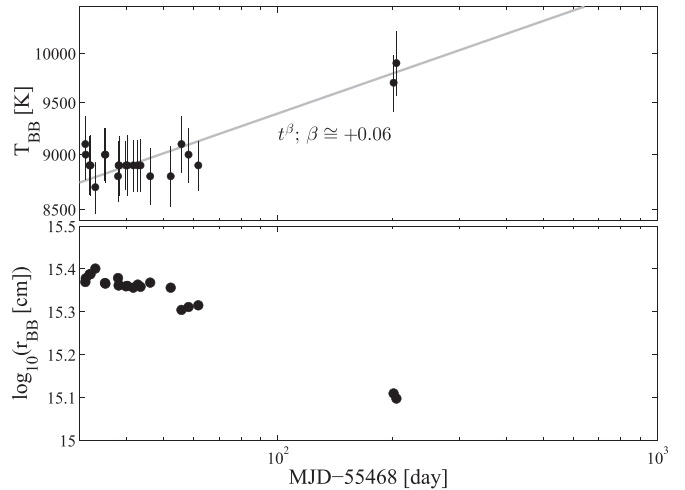

Figure 4. Temperature and radius of a blackbody that best fits the *Swift*-UVOT observations as a function of time. Observations made more than 500 days after maximum light are excluded, as they are significantly affected by the host-galaxy light and we do not yet have a reference image of the host. The gray line shows a power law fitted to the temperature data.

2.3. Swift-UVOT

The Ultra-Violet/Optical Telescope (UVOT; Roming et al. 2005) on board the *Swift* satellite (Gehrels et al. 2004) observed SN 2010jl on several occasions. The data were reduced using standard procedures (e.g., Brown et al. 2009). Flux from the transient was extracted from a 3″ radius aperture, with a correction applied to put the photometry on the standard UVOT system (Poole et al. 2008). The resulting measurements, all of which have been converted to the AB system, are listed in Table 1 and are shown in Figure 1. We caution that these results have not incorporated any contribution from the underlying host galaxy and may therefore overestimate the SN flux at late times. Specifically, the UVOT measurements in Figure 1 near 900 days are heavily contaminated by an underlying star-forming region in the host galaxy.

We fitted a blackbody spectrum to the UVOT measurements as a function of time, and the results are shown in Figure 4. In the fits we corrected the flux measurements for Galactic extinction, assuming $E_{B-V} = 0.027$ mag (Schlegel et al. 1998) and $R_V = 3.08$ (Cardelli et al. 1989). We note that we also tried to fit the blackbody spectrum with E_{B-V} as a free parameter and verified that the best fit is obtained near the Schlegel et al. (1998) value for E_{B-V}. The *Swift*-derived blackbody temperature shows some indications that it is rising in the first ∼200 days after maximum light. However, we caution that deviations from a blackbody caused by spectral lines that are not dealt with in the broadband observations, as well as deviations from a blackbody spectrum (see Section 5.2) and metal-line blanketing, can affect the derived temperature and radius. Therefore, we argue that the quoted temperatures are likely only a lower limit on the effective temperatures.

These temperature measurements differ from those obtained using the spectroscopic observations (Section 2.3). However, due to metal-line blanketing and given that the spectral peak is too blue to be probed by visible-light spectra, we consider both the spectroscopic and UVOT observations to be lower limits on the temperature. The temperature evolution based on the visible-light spectra is opposite to that based on the UVOT observations. However, both evolutions seen in Figures 3 and 4 are very moderate. In Section 5.1 we investigate the effect of

Table 3
Log of *NuSTAR*, *XMM*, and *Chandra* Observations

Inst	ObsID	MJD (day)	Exposure Time (s)	Count Rate (ct ks^{-1})
Chandra	11237	55,522.12	10,046	11.2 ± 1.0
Chandra	11122	55,537.29	19,026	9.64 ± 0.71
Chandra	13199	55,538.16	21,032	11.72 ± 0.74
Chandra	13781	55,852.09	41,020	32.05 ± 0.88
NuSTAR	40002092001	56,205.98	46,000	27.2 ± 0.8
XMM	0700381901	56,232.72	12,914	158 ± 4

Notes. MJD is the modified Julian day. The background-corrected count rate is in the 0.2–10 keV band for *Chandra* and *XMM*, and 3–79 keV for *NuSTAR*. For *Chandra* we used an extraction aperture radius of 3″ and a sky annulus whose inner (outer) radius is 20″ (40″). For *XMM* we used an extraction aperture radius of 32″ and a sky annulus whose inner (outer) radius is 32″ (33″.5). For *NuSTAR* we used an extraction aperture radius of 60″ and a sky annulus whose inner (outer) radius is 60″ (100″). The *XMM* count rate is the combined value from all three instruments. The first three *Chandra* observations were obtained within a time window of 16 days. Here we analyzed the first three observations jointly and refer to them as the first *Chandra* epoch, while *Chandra* ObsID 13781 is referred to as the *Chandra* second epoch.

this uncertainty on our results, and in Section 5.2 we discuss the nature of the decrease in the blackbody radius at late times.

2.4. NuSTAR

NuSTAR is the first hard X-ray focusing satellite (Harrison et al. 2013). Its broad energy range (3–79 keV) allows us to determine the previously unconstrained temperature of the hardest component of the X-ray spectrum. *NuSTAR* observed SN 2010jl on 2012 October 6, roughly 2 yr after the discovery of the SN. We obtained a usable exposure time of 46 ks. This was the first SN observed by the *NuSTAR* "supernovae and target-of-opportunity program." Spectra and images were extracted using the standard *NuSTAR* Data Analysis Software (NuSTARDAS version 0.11.1) and HEASOFT (version 6.13). XSPEC (Arnaud 1996, version 12.8) was used to perform the spectral analysis in combination with the *XMM* data. A summary of the high-energy observations of SN 2010jl is given in Table 3.

2.5. XMM

Shortly after we obtained the *NuSTAR* observations, we triggered *XMM-Newton* for a target-of-opportunity observation (see Table 3) with the goal of determining the bound-free absorption utilizing *XMM*'s good low-energy X-ray response. The observation was carried out during 2012 November 1 for 13 ks, resulting in a usable exposure time of ∼10 ks for the MOS1 and MOS2 detectors and ∼4 ks for the PN detector, after filtering out periods of high background flaring activity. The Science Analysis System software (SAS, version 12) was used for data reduction. Spectral analysis combined with the *NuSTAR* data was performed using XSPEC version 12.8.

2.6. Chandra

Chandra observed the location of SN 2010jl on five epochs (PIs Pooley, Chandra; Chandra et al. 2012a). All the observations except one are public.

Inspection of the *Chandra* images shows emission from the SN position, as well as from another source only about 2″ east of the SN (Figure 5). In order to make sure that the *Chandra* flux measurements are compatible with the other X-ray observations, we used a relatively large aperture of radius 3″. This extraction
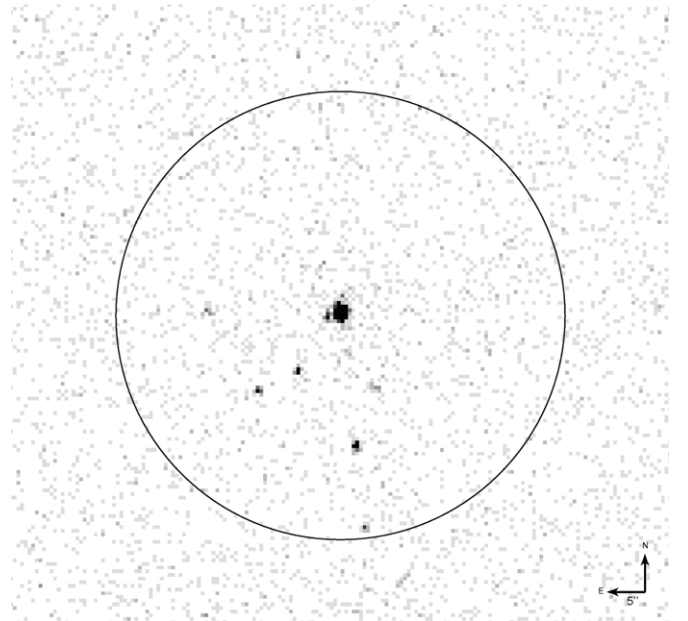

Figure 5. *Chandra* image of SN 2010jl (ObsID 13781). The SN is the bright source at the center. The nearby source is 2″ east of the SN. The black circle has a radius of 30″, similar to the *XMM* extraction region. Several sources are visible within this extraction radius. There are no additional bright sources outside this radius and within 60″ of the SN position (i.e., the *NuSTAR* extraction region).
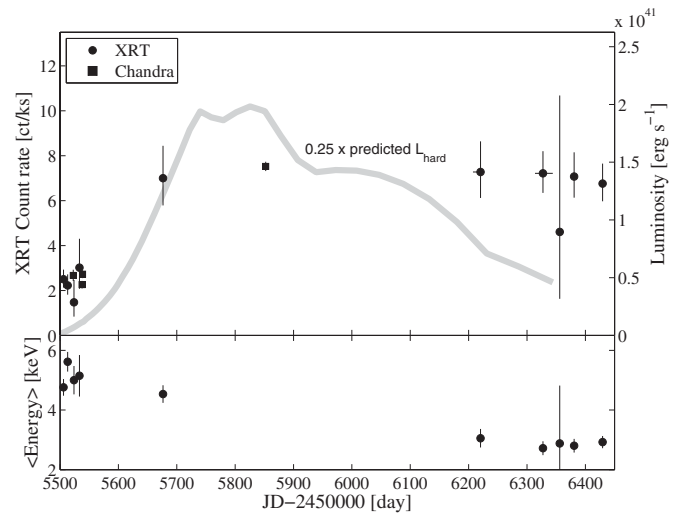

Figure 6. Upper panel: X-ray light curve of SN 2010jl. The left-hand ordinate axis shows the *Swift*-XRT count rate, while the right-hand ordinate axis represents the *Swift* and *Chandra* X-ray luminosity in the 0.2–10 keV band assuming a Galactic neutral hydrogen column density of 3×10^{20} cm^{-2} (Dickey & Lockman 1990) and an X-ray spectrum of the form $n(E) \propto E^{-1}$, where $n(E)$ is the number of photons per unit energy. We note that the unabsorbed luminosity would be a factor of 1.7, 4.5, and 54 times higher for a neutral hydrogen column density of 10^{22}, 10^{23}, and 10^{24} cm^{-2}, respectively. The gray line shows 0.25 times the predicted X-ray luminosity based on Equation (27), assuming $m = 10$ before t_{br} and $m = 4$ afterward (see Section 5.3). The XRT and *Chandra* measurements are contaminated by the nearby source and therefore overestimate the flux by about 10%. Lower panel: the mean X-ray energy of the *Swift*-XRT photons in the 0.2–10 keV range.

aperture contains light from the nearby source. The background was extracted from an annulus with an inner (outer) radius of 20″ (40″). The observations are plotted in Figure 6 and presented in Table 3.

In addition, there are multiple weak sources located within the source extraction regions of *XMM* and *NuSTAR*

Table 4
Swift-XRT Observations

MJD (day)	Exposure Time (ks)	Source (ct)	Background (ct)
55,505.08	1.93	3	2
55,505.15	13.49	15	26
55,505.67	6.70	12	19
55,505.89	4.66	6	19
55,506.08	1.80	0	2

Notes. MJD is the modified Julian day. Source is the number of counts in the 0.2–10 keV band within an aperture radius of $9''$, centered on the source position. Background is the number of counts in the 0.2–10 keV band in an annulus of inner (outer) radius $50''$ ($100''$) around the source. The ratio between the background annulus area and the aperture area is 92.59.

(This table is available in its entirety in a machine-readable form in the online journal. A portion is shown here for guidance regarding its form and content.)

(Figure 5). We use the *Chandra* observation to determine their mean flux and spectrum, and as an additional (known) component while fitting the spectra from *NuSTAR* and *XMM*. The *Chandra* data were analyzed using XSPEC[17] V12.7.1 (Schafer 1991). The Galactic neutral hydrogen column density in the direction of SN 2010jl is $N_H = 3 \times 10^{20}$ cm^{-2} (Dickey & Lockman 1990). All of the nearby sources were fitted jointly with an absorbed power law assuming Galactic absorption. The fit resulted in a photon power-law index of $\Gamma = 1.375$ and a flux of 6.3×10^{-6} photon cm^{-2} s^{-1} in the energy range 0.3–10 keV (χ^2/dof = 12.5/12). The spectra and the contamination by the nearby sources are discussed and modeled in Section 3.

2.7. *Swift*-XRT

The *Swift* X-Ray Telescope (XRT; Burrows et al. 2005) observed SN 2010jl on multiple epochs since the SN discovery. For each *Swift*/XRT image of the SN, we extracted the number of X-ray counts in the 0.2–10 keV band within an aperture of $9''$ radius centered on the SN position. This aperture contains ~50% of the source flux (Moretti et al. 2004). The background count rates were estimated in an annulus around the SN location, with an inner (outer) radius of $50''$ ($100''$). The log of *Swift*-XRT observations, along with the source and background X-ray counts in the individual observations, is listed in Table 4. The binned *Swift*-XRT observations are presented in Figure 6 and listed in Table 5.

3. X-RAY SPECTRA OF SN 2010JL

Chandra et al. (2012a) analyzed the *Chandra* spectra. They found that multiple components are required (e.g., two Mekal[18] spectra; Mewe et al. 1986) in order to obtain a good fit. Based on our modeling described in Section 5, we argue that this SN is powered by interaction of the SN shock with an optically thick CSM. In this case, at least in the first 2 yr after discovery, using Mekal (i.e., optically thin emission) components is not physically justified. It is possible that the good fit obtained by Chandra et al. (2012a) is a result of the large number of free parameters in their model. In addition, it is possible that the

---

[17] http://heasarc.gsfc.nasa.gov/xanadu/xspec/
[18] Mekal is an emission spectrum from hot diffuse gas with lines from Fe, as well as several other elements.

Table 5
Binned *Swift*-XRT Data

⟨MJD⟩ (day)	Range (day)	(day)	CR (counts ks^{-1})	Exp. (ks)	⟨E⟩ (keV)
55,505.5	−0.4	3.6	$2.50^{+0.43}_{-0.37}$	36.02	4.76 ± 0.28
55,512.6	−0.7	4.9	$2.22^{+0.49}_{-0.41}$	26.08	5.62 ± 0.33
55,523.4	−3.3	2.8	$1.47^{+1.0}_{-0.64}$	6.79	5.00 ± 0.48
55,532.7	−3.0	3.0	$3.02^{+1.3}_{-0.94}$	6.63	5.15 ± 0.70
55,675.9	−0.3	3.2	$7.00^{+1.4}_{-1.2}$	9.43	4.53 ± 0.30
56,219.9	−12.9	1.4	$7.28^{+1.4}_{-1.2}$	10.72	3.06 ± 0.31
56,326.9	−13.8	16.7	$7.21^{+1.0}_{-0.87}$	18.85	2.72 ± 0.23
56,355.5	−0.0	0.0	$4.61^{+6.1}_{-3.0}$	0.87	2.88 ± 1.94
56,380.3	−0.0	0.0	$7.07^{+1.1}_{-0.94}$	15.83	2.80 ± 0.23
56,429.1	−2.4	4.4	$6.76^{+0.89}_{-0.79}$	21.60	2.92 ± 0.21

Notes. SN 2010jl binned *Swift*-XRT light curve. ⟨MJD⟩ is the weighted mean modified Julian day of all the observations in a given bin, where the observations are weighted by their exposure times. Range is the time range around ⟨MJD⟩ in which the light curve (Table 4) was binned. CR is the counts rate along with the lower and upper 1σ uncertainties. The source count rates are corrected for extraction aperture losses (50%). ⟨E⟩ is the mean energy of photons within the 0.2–10 keV range and the standard error of the mean.

low-energy component suggested by Chandra et al. (2012a) originates from the nearby (soft) source (see below). Here we attempt to fit physically motivated simple models, with a small number of degrees of freedom.

As mentioned in Section 2.6, the *Chandra* images show several other sources near the position of SN 2010jl. Interestingly, we identify one source only $2''$ from the SN position. We note that the mean photon energies of the primary source (i.e., the SN) and this nearby source are very different, about 4 and 2 keV, respectively. We fitted a two point-spread function (PSF; CALDB, version 4.5.5.1) model to the two sources simultaneously using our own code. We use the *Chandra* 4 keV PSF for the SN, and the 2 keV PSF for the nearby source. This exercise allows us to measure the flux of the nearby source (which is useful as a constraint while analyzing data from other instruments with poorer resolution). This also shows that the nearby source is real and not an artifact of the *Chandra* PSF. We find that in ObsID 11237 the nearby source contributes 14.1% of the total flux. We also find that this nearby source is consistent with being constant in time (over the *Chandra* epochs) and has a mean count rate of 0.0010 counts s^{-1} (15% error) in the 0.2–10 keV band.

We speculate that this source interfered with the X-ray spectral fitting reported by Chandra et al. (2012a). In fact, using an extraction aperture that does not contain the nearby source changes the result relative to an extraction with a bigger aperture that contains the second source. Therefore, in order to minimize the contamination, we manually selected a small aperture ($3''$ radius) with minimal second-source flux (i.e., the aperture was shifted from the source center to exclude photons from the nearby source).

Table 6 gives a summary of our best-fit models to the various X-ray observations. We note that some of these models have strong degeneracies between the parameters. Therefore, it is hard to interpret the X-ray spectra. Moreover, we still lack a good physical understanding of the X-ray spectra from optically thick shocks. Given these caveats, in Table 6 we fit several models, some of which are motivated by our modeling of the optical light curve, presented in Section 5.3. The *NuSTAR* + *XMM* spectral
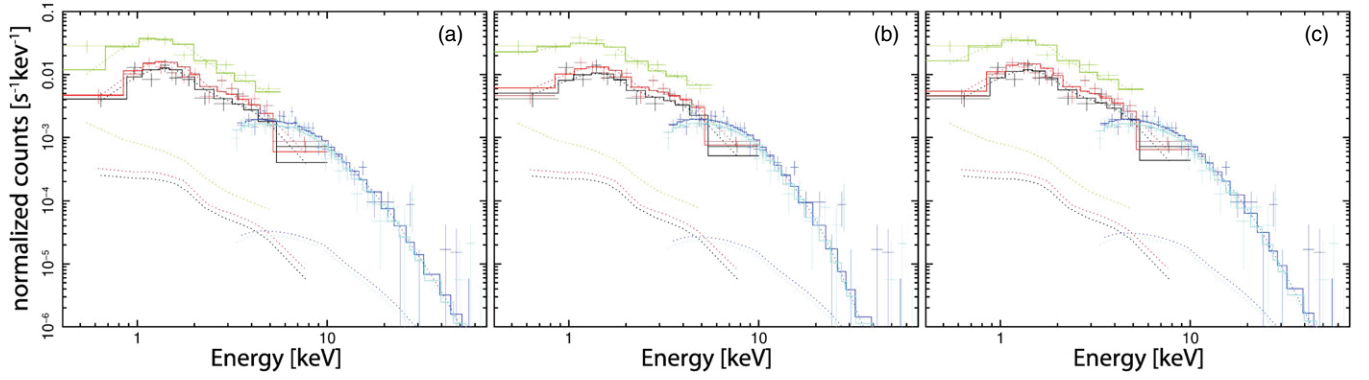
Figure 7. Panel (a): best-fit Mekal (zvphabs*mekal) to the combined *NuSTAR*+*XMM* observation. The model consists of two components: The lower dotted lines represent the fixed power-law model of the faint nearby sources (see text), and the upper dotted lines represent the zvphabs*mekal best-fit model to the SN 2010jl X-ray spectrum. The solid lines (stairs) show the best combined fit for each instrument, while the plus signs show the data with error bars. The instruments are *NuSTAR* FPM A (blue), *NuSTAR* FPM B (cyan), *XMM* PN (green), *XMM* MOS1 (black), and *XMM* MOS2 (red). The fit parameters are listed in Table 6. Panel (b): like panel (a) but for zvphabs*powerlaw*spexpcut. Panel (c): like panel (a) but for zvphabs*powerlaw*spexpcut with fixed $\Gamma = 1$.

Table 6
Spectral Modeling of the X-Ray Data

Instruments	ObsIDs	MJD	Counts	Model		
			(cnt)	Parameters	Val	C-stat/dof (goodness)
Chandra	11237,11122,13199	55,536	485	zphabs*zbb		33.0/34 (0.76)
				N_H	20×10^{22} cm^{-2} (frozen)	
				kT	$3.4^{+1.2}_{-0.7}$ keV	
				norm	$(4.4^{+4.0}_{-1.5}) \times 10^{-5}$	
				zphabs*powerlaw*spexpcut		no fit
				kT	1.5 keV (frozen)	
Chandra	13781	55,852	1257	zphabs*zbb		73.5/76 (0.20)
				N_H	$(0.7^{+0.3}_{-0.2}) \times 10^{22}$ cm^{-2}	
				kT	$3.4^{+0.7}_{-0.5}$ keV	
				norm	$(4.7^{+2.5}_{-1.3}) \times 10^{-5}$	
				zphabs*powerlaw*spexpcut		81.4/76 (0.36)
				N_H	$0.99^{+0.43}_{-0.39}) \times 10^{22}$ cm^{-2}	
				kT	15 keV (frozen)	
				Γ	-0.45 ± 0.23	
				norm	$(1.41^{+0.65}_{-0.44}) \times 10^{-5}$	
NuSTAR+*XMM*	(Table 3)			zvphabs*mekal		120.6/95 (0.79)
	Ignoring faint sources			N_H	$(1.1^{+0.2}_{-0.2}) \times 10^{22}$ cm^{-2}	
				kT	$18.2^{+6.2}_{-4.0}$ keV	
	Faint sources removed			zvphabs*mekal		119.7/94 (0.73)
				N_H	$(1.1^{+0.3}_{-0.2}) \times 10^{22}$ cm^{-2}	
				kT	$17.7^{+6.1}_{-3.9}$ keV	
	Faint sources removed			zvphabs*powerlaw*spexpcut		94.0/94 (0.16)
				N_H	$(0.28^{+0.21}_{-0.17}) \times 10^{22}$ cm^{-2}	
				kT	$(5.6^{+1.9}_{-1.2})$ keV	
				Γ	$0.45^{+0.26}_{-0.26}$	
	Faint sources removed			zvphabs*powerlaw*spexpcut		105.5/95 (0.43)
				N_H	$(0.65^{+0.16}_{-0.14}) \times 10^{22}$ cm^{-2}	
				kT	$(10.1^{+2.1}_{-1.6})$ keV	
				Γ	1 (frozen)	

Notes. Separated by horizontal lines are the different models fitted to the three epochs of X-ray spectra. Models that include redshift (e.g., zphabs, zbb) use the SN redshift as a frozen parameter; spexpcut is an exponential cutoff model of the form $\exp(-[E/kT]^\gamma)$, where we freeze $\gamma = 1$; and powerlaw is a power-law model of the form $\propto E^{-\Gamma}$, where the normalization parameter has units of photons keV^{-1} cm^{-2} s^{-1} at 1 keV. Goodness is calculated using the `Xspec` "goodness 1000" command (i.e., the fraction of realizations with C-statistic < best-fit C-statistic). The *NuSTAR*+*XMM* fits have two versions. Those with "Ignoring faint sources" in the second column are fits for all the photons within the large extraction apertures of *NuSTAR* and *XMM*. This fit is contaminated by the faint sources within the PSF (Figure 5). In fits marked by "Faint sources removed" we added a frozen component to the model that takes into account the combined spectrum of all the faint sources within the PSF, as measured in the *Chandra* images (see Section 2.6).
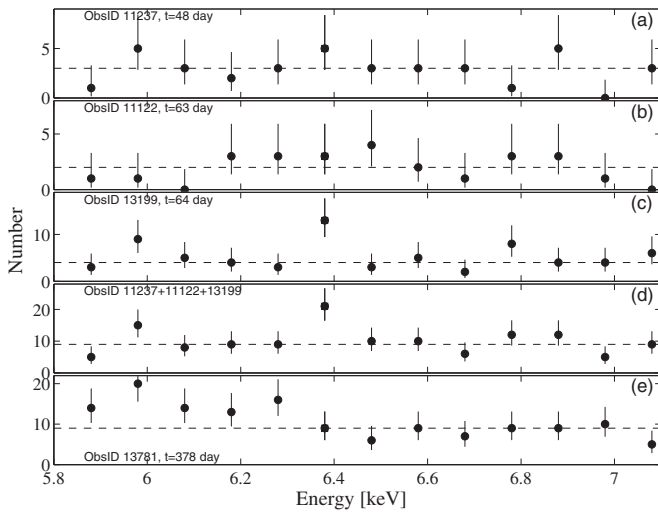
Figure 8. *Chandra* spectra of SN 2010jl around the Kα-line energy. The spectra are uncorrected for instrumental sensitivity. The first three panels (a–c) show the individual first three observations. Panel (d) shows the coaddition of the first three observations, designated as the first *Chandra* epoch. Panel (e) presents the second *Chandra* epoch. The time relative to MJD 55,474 is marked on each plot. The bin size is 0.1 keV, which corresponds to a velocity of 4700 km s^{-1}. Measurements indicated by squares show the bin centered around 6.38 keV (i.e., the rest-frame energy of the Kα line).

fits are shown in Figure 7. The models we use are either Mekal spectra or power laws with an exponential cutoff that corresponds to the gas temperature. In addition, the models include bound-free absorption due to solar-metallicity gas.

Chandra et al. (2012a) reported the detection of a 6.38 keV iron Kα emission line in the *Chandra* spectrum taken in the first year. In Figure 8 we show the *Chandra* spectra, uncorrected for instrumental sensitivity, around the Kα energy. The third observation (ObsID 13199) and the coaddition of the first three observations (i.e., first epoch; ObsIDs 11237, 11122, 13199) show a possible detection of the Kα emission line. In order to estimate the line properties and significance, we used the maximum-likelihood technique to fit a Gaussian profile to the line. We find that the best-fit rest-frame energy (assuming $z = 0.0107$) is $6.41^{+0.03}_{-0.04}$ keV, the line width is $\sigma = 0.033^{+0.19}_{-0.032}$ keV (this corresponds to $\sigma = 1540^{+8800}_{-1500}$ km s^{-1}), and the line flux is $(3.6^{+5.8}_{-3.0}) \times 10^{-5}$ counts s^{-1}. We note that the ACIS-S energy resolution around 6.4 keV is about 280 eV, which corresponds to a velocity of 13,000 km s^{-1}. Therefore, our best-fit line width prefers an unresolved spectral line (i.e., zero velocity broadening). We also find that there is a 2.5% probability that the Kα line is not real.

4. MODEL

Here we outline a theoretical framework to analyze the observations in the context of an interaction model. We compare this model with the observations in Section 5. An important caveat for our model is that it assumes spherical symmetry, which is reasonable only if the deviations from spherical symmetry are of order unity.

Our modeling strategy is similar to the one described by Svirski et al. (2012), but it is more general in the sense that we do not assume the values of the CSM radial density distribution and ejecta velocity distribution. A qualitative outline of the model is presented in Section 4.1. Section 4.2 presents the model quantitatively and describes the bolometric luminosity

as a function of time. In Section 4.3 we discuss the possibility of detecting radio emission, and Section 4.4 discusses the properties of the X-ray emission.

4.1. Qualitative Description of the Model

A brief outline of the model is as follows. After the SN shock moves beyond the stellar surface, it propagates in an optically thick CSM and some of its kinetic energy is converted into optical photons (UV to IR). The relevant source of opacity is mainly Thomson scattering, which is independent of wavelength. If the Thomson optical depth τ is large enough, the photons are trapped and the shock energy is mediated by photons—photons diffuse out, scattering upstream electrons and accelerating them. A radiation-mediated shock "breaks down" or "breaks out" (i.e., radiation escapes ahead of the shock) when photons diffuse ahead of the shock faster than the shock propagates. This happens when $\tau \approx c/v_s$ (Weaver 1976; and see discussion for the case of wind breakout in Ofek et al. 2010). Here v_s is the shock velocity, and c is the speed of light.

Katz et al. (2011) and Murase et al. (2011) showed that if there is a sufficiently large amount of CSM above the shock-breakout radius, the shock will transform from being radiation mediated to collisionless (i.e., the photons are no longer trapped). At this time the shock (and ejecta) is moving through the CSM and its kinetic energy is converted to radiation at a rate of $\epsilon(\rho v_s^2/2)(4\pi r_s^2 v_s)$, where ϵ is the efficiency, ρ is the CSM density, and r_s is the shock radius (e.g., Svirski et al. 2012). The time dependences of r_s and v_s, while the ejecta and CSM are interacting, are known from self-similar solutions of the hydrodynamical equations (Chevalier 1982).

Later on, when the shock runs over a mass of CSM equivalent to the ejecta mass, the shock will go into a new phase of either conservation of energy if the density is low enough and the gas cannot cool quickly (i.e., the Sedov–Taylor phase), or conservation of momentum if the gas can radiate its energy by fast cooling (i.e., the snow-plow phase). In either case, the light curve in this final stage will be characterized by a steeper decay rate (Svirski et al. 2012).

The observables in this approach are the light-curve rise time, the luminosity and its decay rate, the time of power-law break in the light curve, and the shock velocity at late times as measured from the hard X-ray observations. These observables allow us to solve for the shock radius and velocity as a function of time, the CSM density profile, and the total mass; they also provide a consistency test.

4.2. The Optical Light Curve

An SN explosion embedded in CSM with optical depth in excess of $\sim c/v_s$, where c is the speed of light and v_s is the SN shock velocity, will have a shock breakout within the optically thick CSM. The analytical theory behind this was presented by Ofek et al. (2010), Chevalier & Irwin (2011), Balberg & Loeb (2011), Ginzburg & Balberg (2012), Moriya & Tominaga (2012), and Svirski et al. (2012), while simulations of such scenarios were presented by Falk & Arnett (1973, 1977), among others. Here we review the theory and extend it to a general CSM power-law density profile and general ejecta velocity power-law distributions.

Following Chevalier (1982), we assume that the expanding ejecta have a spherically symmetric power-law velocity

distribution of the form

$$\rho_{\rm ej} = t^{-3}\left(\frac{r}{tg}\right)^{-m}. \qquad (1)$$

Here $\rho_{\rm ej}$ is the ejecta density, t is the time, r is the radius, m is the power-law index of the velocity distribution, and g is a normalization constant. This model is justified because the outer density profile of massive stars can likely be approximated as a power law (e.g., Nomoto & Sugimoto 1972). We expect $m \approx 10$ for progenitor stars with a radiative envelope, and $m \approx 12$ for progenitor stars with a convective envelope (e.g., Matzner & McKee 1999). We assume that the ejecta are expanding into a CSM with a spherically symmetric power-law density profile of the form

$$\rho_{\rm csm} = K r^{-w}, \qquad (2)$$

where w is the power-law index and K is the normalization.[19] In a wind profile, $w = 2$, $K = \dot{M}/(4\pi v_{\rm CSM})$ is called the mass-loading parameter with units of g cm^{-1} (where $v_{\rm CSM}$ is the CSM or wind velocity), and $\dot{M}$ is the mass-loss rate. We note that even if the CSM is ejected in a single outburst, we expect the CSM to spread over a wide range of radii since the ejecta probably have a wide range of velocities. Given these assumptions, Chevalier (1982) showed that the forward-shock radius is given by

$$r_{\rm s} = \left(\frac{Ag^m}{K}\right)^{1/(m-w)} t^{(m-3)/(m-w)}$$
$$\equiv r_0\left(\frac{t}{t_0}\right)^{(m-3)/(m-w)}, \qquad (3)$$

where A is a constant derived from the self-similar solution. The second part of the equation simply absorbs the coefficients into arbitrary r_0 and t_0. By differentiating Equation (3), we get the forward-shock velocity as a function of time,

$$v_{\rm s} = \frac{m-3}{m-w}\left(\frac{Ag^n}{K}\right)^{1/(m-w)} t^{(w-3)/(m-w)}$$
$$\equiv v_0\left(\frac{t}{t_0}\right)^{(w-3)/(m-w)}, \qquad (4)$$

where

$$v_0 \equiv \frac{m-3}{m-w}\frac{r_0}{t_0}. \qquad (5)$$

The shock breakout in a CSM environment occurs when the Thomson optical depth is

$$\tau \approx c/v_{\rm bo}, \qquad (6)$$

where $v_{\rm bo}$ is the shock velocity at breakout (e.g., Weaver 1976). The expression for the Thomson optical depth, assuming $w > 1$, is

$$\tau = \int_{r_{\rm s}}^{\infty} \rho\kappa\,dr = \frac{\kappa K}{w-1}r_{\rm s}^{1-w}, \qquad (7)$$

where $r_{\rm s}$ is the forward-shock radius and κ is the opacity. We note that for $w = 2$, Balberg & Loeb (2011) showed that the total optical depth (taking into account the reverse-shock contribution) is a factor of 1.55 times larger. Chevalier (2013) argues that at relatively late times, if the CSM density is low, the reverse shock may dominate the X-ray emission. In this case the effective optical depth may be even higher. Effectively, this uncertainty can be absorbed into the uncertainty in the

opacity κ, which is discussed in Section 5. We note that our main conclusions do not depend on the late-time observations. From Equations (6) and (7) we can derive an expression for K,

$$K \approx \frac{c}{v_{\rm bo}\kappa}(w-1)r_{\rm bo}^{w-1}$$
$$= \frac{c}{\kappa}(w-1)\left(\frac{m-w}{m-3}\right)^{w-1} v_{\rm bo}^{w-2} t_{\rm bo}^{w-1}, \qquad (8)$$

where the last step is obtained using Equation (5). Here $r_{\rm bo}$, $v_{\rm bo}$, and $t_{\rm bo}$ are the radius, velocity, and timescale of the shock breakout, respectively (replacing r_0, v_0, and t_0).

The integrated CSM mass within radius r or time t, assuming $w < 3$ and star radius $r_* \ll r$, is given by

$$M = \int_0^r 4\pi r^2 K r^{-w}\,dr = \frac{4\pi K}{3-w}r^{3-w}$$
$$= \frac{4\pi K}{3-w}\left(\frac{m-w}{m-3}\right)^{3-w} v_{\rm bo}^{3-w} t_{\rm bo}^{(3-w)^2/(m-w)} t^{(3-w)(m-3)/(m-w)}. \qquad (9)$$

Assuming fast cooling, following the shock breakout the kinetic energy is converted into radiation (bolometric luminosity) at a rate of

$$L = 2\pi\epsilon r_{\rm s}^2 \rho v_{\rm s}^3. \qquad (10)$$

The value of the efficiency factor, ϵ, is discussed in Section 5. We note that Equation (10) assumes that $v_{\rm s} \gg v_{\rm CSM}$. Substituting the expressions for $r_{\rm s}$ (Equation (3)), ρ (Equation (2)), and $v_{\rm s}$ (Equation (4)) into Equation (10), we get

$$L = L_0 t^{\alpha}, \qquad (11)$$

where

$$\alpha \equiv \frac{(2-w)(m-3)+3(w-3)}{m-w} \qquad (12)$$

and

$$L_0 \equiv 2\pi\epsilon K r_{\rm bo}^{2-w} v_{\rm bo}^3 t_{\rm bo}^{-\alpha}. \qquad (13)$$

Using Equation (5), we can remove $r_{\rm bo}$ from Equation (10) and get

$$L_0 = 2\pi\epsilon K\left(\frac{m-w}{m-3}\right)^{2-w} v_{\rm bo}^{5-w} t_{\rm bo}^{2-w-\alpha}. \qquad (14)$$

Equation (11) was derived by Svirski et al. (2012) for the special case of $w = 2$ and $m = 12, 7, 4$.

Equation (11) provides a description of the light curve following the shock breakout, assuming $w < 3$ and $m > 4$ (for radiative shock). However, another condition is that $w \geqslant 2$. The reason is that if $w < 2$, then the diffusion timescale diverges, and therefore the shock will break out near the edge of the CSM. In this case we will not see a light curve with a power-law decay (i.e., Equation (11)) lasting for a long period of time as seen in Figure 1. Therefore, $w < 2$ is not a relevant solution for SN 2010jl. Figure 9 presents the value of α as a function of m and w. We are not aware of a relevant self-similar solution[20] for $w > 3$.

Equation (11) is correct only if the shock is in the fast-cooling regime. The free–free cooling timescale is

$$t_{\rm ff,cool} \approx 1.8 \times 10^{15}\left(\frac{T}{10^8\,{\rm K}}\right)^{1/2}\left(\frac{n}{1\,{\rm cm}^{-3}}\right)^{-1} Z^{-2}\,{\rm s}, \qquad (15)$$

---

[19] Chevalier (1982) denotes K by q and w by s.

[20] The Waxman & Shvarts (1993) solution does not correspond to fast cooling, which is the case here.
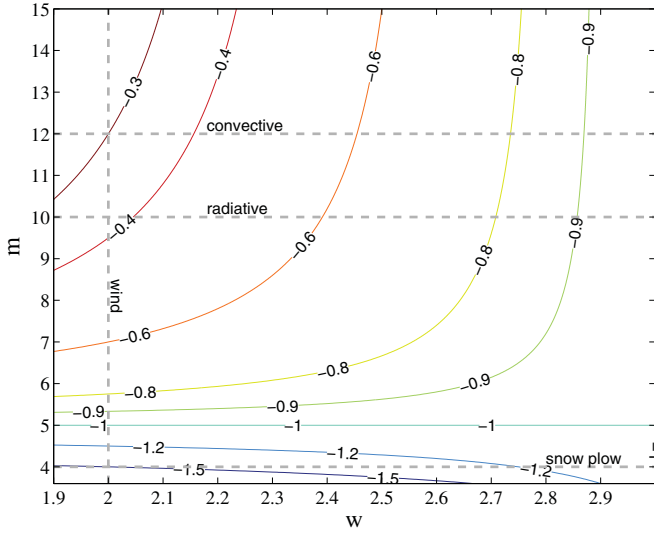
Figure 9. Contours of the value of α (i.e., power-law index of the early-time light curve; Equation (12)) as a function of m and w. The dashed gray lines show several (labeled) interesting values of m and w.

(A color version of this figure is available in the online journal.)

where Z is the atomic number of the atom and n is the particle density given by

$$n = \frac{K}{\langle \mu_p \rangle m_p} r^{-w}, \tag{16}$$

where $\langle \mu_p \rangle$ is the mean number of nucleons per particle (mean molecular weight) and m_p the proton mass. The criterion for fast cooling is that $t_{\rm ff,cool} \lesssim t$. Therefore, for timescales of a year $(3 \times 10^7 \, {\rm s})$, fast cooling requires $n \gtrsim 6 \times 10^7 \, {\rm cm}^{-3}$.

Several other important relations can be derived. By rearranging Equation (8), we get

$$t_{\rm bo} = \left[\frac{c}{\kappa K}(w-1) \right]^{1/(1-w)} \frac{m-3}{m-w} v_{\rm bo}^{(w-2)/(1-w)}. \tag{17}$$

From Equation (14) we find

$$K = \frac{L_0}{2\pi\epsilon} \left(\frac{m-w}{m-3} \right)^{w-2} v_{\rm bo}^{w-5} t_{\rm bo}^{\alpha+w-2}, \tag{18}$$

and by substituting Equation (18) into Equation (17) we get

$$t_{\rm bo} = \left[2\pi\epsilon \frac{m-w}{m-3}(w-1)\frac{c}{\kappa L_0} v_{\rm bo}^3 \right]^{1/(\alpha-1)}, \tag{19}$$

or alternatively

$$v_{\rm bo} = t_{\rm bo}^{(\alpha-1)/3} \left[2\pi\epsilon \frac{m-w}{m-3}(w-1)\frac{c}{\kappa L_0} \right]^{-1/3}. \tag{20}$$

These relations suggest that in SNe that are powered by interaction we expect to detect correlations between the SN rise time, its peak luminosity, and shock velocity. We note that this can be used to test the hypothesis that the super-luminous SNe (see review in Gal-Yam 2012) are powered by interaction of their ejecta and CSM (e.g., Quimby et al. 2011). As far as we can tell, such correlations are not expected in the context of other models (e.g., Kasen & Bildsten 2010). Furthermore, by inserting Equations (8) and (20) into Equation (9), we get the

total CSM mass swept by the shock up to time t as a function of the observables (e.g., L_0, $t_{\rm bo}$),

$$M = 4\pi c \left(\frac{m-w}{m-3} \right)^{5/3} \frac{(w-1)^{2/3}}{3-w} \left(\frac{2\pi c\epsilon}{L_0} \right)^{-1/3} \kappa^{-2/3}$$
$$\times t_{\rm bo}^{[(m-w)(3w-4)+(w-3)(3w-6)+(2-w)(m-3)]/[3(m-w)]}$$
$$\times t^{(3-m)(w-3)/(m-w)}. \tag{21}$$

For the specific case of $w = 2$ and $m = 10$ we can write this as

$$M \approx 15.1 \left(\frac{\epsilon}{0.25} \right)^{-1/3} \left(\frac{L_0}{10^{46} \, {\rm erg\,s}^{-1}} \right)^{1/3} \left(\frac{\kappa}{0.34 \, {\rm cm}^2 \, {\rm gr}^{-1}} \right)^{-2/3}$$
$$\times \left(\frac{t_{\rm bo}}{20 \, {\rm day}} \right)^{2/3} \left(\frac{t}{365 \, {\rm day}} \right)^{7/8} M_\odot. \tag{22}$$

We note that L_0 is the luminosity evaluated at time of 1 s rather than $t_{\rm bo}$ (see definition in Equation (11)). Additional relations can be derived, including relations that depend on $v_{\rm bo}$ and/or the integrated luminosity (i.e., $\int L dt = L_0 t^{\alpha+1}/[\alpha + 1]$), rather than on L_0. However, some of these relations are algebraically long, and we do not provide them here.

At later times when the mass of the CSM accumulated by the ejecta is equivalent to the ejecta mass, the light curve evolves in a different way than described so far. In the case of fast cooling (i.e., cooling timescale [e.g., Equation (15)] is shorter than the dynamical timescale), the system enters the snow-plow phase. While at these times the reverse shock is absent and the formalism of Chevalier (1982) does not apply, we can obtain the correct time dependence by using an artificial value of m (no longer related to the ejecta profile). In this snow-plow phase the light curve evolves effectively with $m = 4$ regardless of the value of w (see Svirski et al. 2012). The reason is that, while in this case the energy is radiated away, the momentum is conserved, and from momentum conservation $\rho r^3 v \approx$ constant, we get $\rho \propto v^{-4}$, hence $m = 4$. If the shock is slowly cooling, we enter the Sedov-Taylor phase and the light curve will drop rapidly.

Figure 9 suggests that for $m = 4$, $\alpha \approx -3/2$, with relatively weak dependence on the value of w. However, the exact value of α is sensitive to the value of m, and for m slightly lower than 4, α can change dramatically. In any case, once the swept-up CSM mass is comparable to the ejected mass, we expect substantially more rapid decline of the bolometric emission.

4.3. Visibility of a Radio Signal

Given the CSM density profile, we can calculate some additional properties. The column density, assuming $w > 1$, between radius r and infinity (i.e., the observer) is

$$N = \int_r^\infty \frac{K}{\langle \mu_p \rangle m_p} r^{-w} dr = \frac{K}{\langle \mu_p \rangle m_p(w-1)} r^{1-w}. \tag{23}$$

The free–free optical depth between the shock region and the observer is given by (e.g., Lang 1999, Equation (1.223); Ofek et al. 2013a)

$$\tau_{\rm ff} \approx 8.5 \times 10^{-28} T_{\rm e,4}^{-1.35} v_{10}^{-2.1} \int_r^\infty n_e^2 dr$$
$$\cong 8.5 \times 10^{-28} T_{\rm e,4}^{-1.35} v_{10}^{-2.1} \frac{K^2}{\langle \mu_p \rangle^2 m_p^2 (2w-1)} r^{1-2w}, \tag{24}$$

where $T_{e,4}$ is the electron temperature in units of 10^4 K and ν_{10} is the frequency in units of 10 GHz. Note that r is measured in cm, and that the last expression is valid for $w > 1/2$. If $\tau_{ff} \gg 1$, a radio signal is not expected (see Murase et al. 2013 for discussions).

4.4. High-energy Emission

NuSTAR opens the hard X-ray band for discovery. Specifically, the shock temperatures associated with typical SN shock velocities ($\sim 10^4$ km s^{-1}) are above 10 keV. Therefore, if the shock is in an optically thin region, the X-ray temperature constitutes a reliable measurement of the shock velocity. The shock velocity depends on the shock temperature (kT) and, assuming an equation of state with $\gamma = 5/3$ and an equilibrium between the electrons and protons, is given by (e.g., Gnat & Sternberg 2009)

$$v_{sh} \approx \sqrt{\frac{16kT}{3\langle\mu_p\rangle m_p}}$$
$$\approx 2920\left(\frac{\langle\mu_p\rangle}{0.6}\right)^{-1/2}\left(\frac{kT}{10\,keV}\right)^{1/2}\,km\,s^{-1}. \quad (25)$$

If equilibrium between the electrons and protons is not present, as expected in SN remnants (e.g., Itoh 1978; Draine & Mckee 1993; Ghavamian et al. 2013), then Equation (25) gives a lower limit on the shock velocity. We note that the expected equilibrium timescale between the protons and electrons is of order $6 \times 10^8 (v_s/3000\,km\,s^{-1})^3 n_e^{-1}$ s, where n_e is the electron density in cm^{-3} (i.e., roughly given by Equation (16); Ghavamian et al. 2013).

However, if the Thomson optical depth is larger than a few, the X-ray emission becomes more complicated. Katz et al. (2011) and Murase et al. (2011) showed that after the shock breakout in a wind CSM environment, the shock transforms from being radiation dominated to collisionless, and hard X-ray emission should be generated. However, Chevalier & Irwin (2012) and Svirski et al. (2012) argued that the hard X-ray photons will be Comptonized to lower energies, and that when the optical depth is large the X-ray spectrum will have a cutoff above an energy of $\sim m_e c^2/\tau^2$. According to Svirski et al. (2012), the observed energy cutoff of the X-ray photons will be

$$k_B T_{x,obs} \approx \min\left[\frac{m_e c^2}{\tau^2}, \frac{3}{16}\mu_p m_p v_s^2\right], \quad (26)$$

where the second term in the minimum function is the shock temperature from Equation (25).

Ignoring bound-free absorption, Svirski et al. (2012) estimated that the X-ray luminosity is roughly given by

$$L_X(t) \approx L(t)\frac{T_{x,obs}(t)}{T_e(t)}\min\left[1, \frac{\epsilon^{ff}}{\epsilon^{IC}}(t)\right]. \quad (27)$$

Here ϵ^{ff} and ϵ^{IC} are the free–free and inverse-Compton cooling efficiencies, respectively (see Chevalier & Irwin 2012; Svirski et al. 2012), and T_e is the electron temperature (Equation (25)). Equation (27) neglects the effect of bound-free absorption and therefore should be regarded as an upper limit. Furthermore, we note that there is no agreement between different theoretical models on the exact X-ray spectral and flux evolution.

Chevalier & Irwin (2012) define[21] an ionization parameter as $\xi = L/(nr^2)$. This definition is only valid when material above

the shock is optically thin. When the optical depth (Equation (7)) is larger than unity, one needs to take into account the fact that the photons diffuse out slower than the speed of light. Since the effective outward-diffusion speed of the photons is $\sim c/\tau$, we define the ionization parameter as

$$\xi \sim \frac{L}{nr^2}\max\left[\tau, 1\right]. \quad (28)$$

However, we stress that this is only an order-of-magnitude estimate of the ionization parameter. Chevalier & Irwin (2012) argue that if the ionization parameter is larger than $\sim 10^4$, then all the metals (which dominate the bound-free absorption) will be completely ionized, and for $\xi \gtrsim 10^2$ the CNO elements will be completely ionized. Here, an important caveat is that it is not clear if the estimate of Chevalier & Irwin (2012) is valid for high optical depth.

5. MODELING THE OBSERVATIONS

Integrating the visible-light luminosity of SN 2010jl gives a lower limit on its radiated energy in the first 3 yr of $> 9\times10^{50}$ erg. This is among the highest radiated bolometric energies observed for any SN (e.g., Rest et al. 2011). This fact, along with the long-term X-ray emission, and emission lines seen in the optical spectra, suggests that SN 2010jl is powered by interaction of the SN ejecta with CSM. Therefore, here we attempt to understand the SN observations with the model described in Section 4.

In Section 5.1 we discuss the modeling of the first-year optical light curves; we show that the model presented in Section 4 describes the observations well, and that it requires a CSM mass in excess of about $10\,M_\odot$. Section 5.2 deals with the nature of the break in the optical light curve and the slope after the break, and in Section 5.3 we verify the consistency of the X-ray observations with our model.

5.1. Early Optical Light Curve

In our model, the rise time is governed by the shock-breakout timescale, and the light curve following shock breakout is given by Equation (11) with $m \approx 10$–12 at early times and $m \approx 4$ at late times. Alternatively, $m \approx 10$–12 and w changes with radius. As a reminder, we note that the value of m at early times is related to the polytropic structure of the stellar envelope (e.g., Matzner & McKee 1999), while $m = 4$ at late times is obtained from conservation of momentum (Section 4.2).

Figure 1 suggests that the light curve of SN 2010jl can be described as a broken power law, with the break between 180 and 340 days after maximum light. Since both Figure 3 and Figure 4 suggest that the temperature in the first year was roughly constant and close to 9000 K, the bolometric correction is rather small[22] and constant. Here we adopt a constant bolometric correction of -0.27 mag, which corresponds to a blackbody spectrum with $T = 9000$ K. We apply this bolometric correction to the PTF R-band data to obtain the bolometric light curve. Later we test the stability of our solution to this assumption.

A power-law fit depends on the temporal zero point, which in our model is roughly the time of maximum luminosity minus the shock-breakout timescale. However, since the shock-breakout timescale is related to the light-curve rise time, and since we do not have good constraints on the light-curve rise time, we

---

[21] The formal definition of the ionization parameter is different, but the definition used by Chevalier & Irwin (2012) is proportional to the ionization parameter and is used self-consistently.

[22] The bolometric correction for the PTF R-band magnitude is about -0.06, -0.27, and -0.60 mag for blackbody temperatures of 7500, 9000, and 11,000 K, respectively.
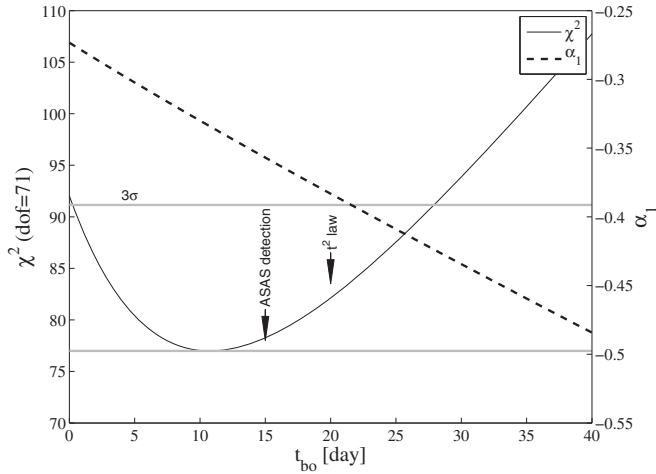
Figure 10. χ^2 (solid line) of the fit of $L_{0,\mathrm{obs}}([t + t_{\mathrm{bo}}]/t_{\mathrm{bo}})^\alpha$ as a function of t_{bo}. The gray horizontal lines show the minimum χ^2 and the 3σ confidence level assuming three free parameters. The dashed line shows the value of α_1 (the power-law index of the optical slope in the first year) as a function of t_{bo}, where its values are presented in the right-hand ordinate axis.

Figure 11. Solutions of Equation (19) as a function of t_{bo} and v_{bo} for various values of m, given the measured values of α_1 (and hence w) and L_0 as a function of t_{bo} (i.e., Figure 10). Also shown, in blue contours, are lines of equal CSM mass within the break radius (M_{br}), assuming $t_{\mathrm{br}} = 300$ day. The number above each contour indicates the mass in units of the solar mass. These solutions assume $\kappa = 0.34$ cm^2 g^{-1} and $\epsilon = 1/4$. Pentagons, circles, squares, and triangles show the positions along the various lines in which $w = 1.95$, 2.0, 2.05, and 2.15, respectively. As explained in Section 4, our model is valid only for $w \geqslant 2$, and $w < 2$ can be ruled out based on the fact that the light curve has a power-law shape with small power-law index (≈ -0.4) for about a year.

(A color version of this figure is available in the online journal.)

have to estimate the shock-breakout timescale in a different way. Therefore, we fitted the first-year PTF luminosity measurements with a power law of the form $L_{0,\mathrm{obs}}([t + t_{\mathrm{bo}}]/t_{\mathrm{bo}})^\alpha$, where t is measured relative to the ASAS I-band maximum light (MJD 55,494). Figure 10 shows the fit χ^2, as well as α_1, as a function of t_{bo}. Here α_1 is the power-law index of the bolometric light curve in the first year after maximum light. The black arrows indicate t_{bo} at which the first ASAS detection was obtained, and t_{bo} derived by fitting the first three ASAS I-band measurements with a t^2 law (e.g., Nugent et al. 2011). The fit prefers $t_{\mathrm{bo}} \approx 10$ day, but $t_{\mathrm{bo}} \lesssim 25$ day is acceptable, while the ASAS early detection indicates $t_{\mathrm{bo}} > 15$ day.

Given specific values of κ, m, α, w, and L_0, Equation (19) shows that there is a relation between t_{bo} and v_{bo}. Moreover, based on Figure 10 we know that $15 \lesssim t_{\mathrm{bo}} \lesssim 25$ day. Figure 11 shows the solutions of Equation (19) as a function of t_{bo} and v_{bo} for various values of m, given the measured values of α_1 (and hence w) and L_0 as a function of t_{bo} (i.e., Figure 10). Also shown, in blue contours, are lines of equal CSM mass within the break radius (M_{br}). Here the break radius is defined as the radius of the shock at 300 days—roughly when the observed break in the power-law light curve is detected. Regardless of the exact values of m, t_{bo}, and v_{bo}, Figure 11 shows that the CSM mass $M_{\mathrm{br}} \gtrsim 10\,M_\odot$ (see also Equations (21) and (22)). It also suggests that $M_{\mathrm{br}} \lesssim 16\,M_\odot$, but the upper limit is somewhat weaker due to several uncertainties that are discussed next.

Assuming $\epsilon = 1/4$ and $\kappa = 0.34$ cm^2 g^{-1}, Table 7 presents the measured values of L_0 and α and the calculated values of w, K, r_{bo}, v_{bo}, and M_{br}, as a function of the assumed t_{bo} and m. Regardless of the exact value of t_{bo}, we find that $2 \lesssim w \lesssim 2.2$—close to the value expected from a wind profile. We note that our approach allows us to measure w rather than assume its value. For the rest of the discussion we will adopt $t_{\mathrm{bo}} = 20$ days and $m = 10$. In this case, the value of K is translated to a mass-loss rate of

$$\dot{M} \approx 0.8 \frac{v_{\mathrm{CSM}}}{300\,\mathrm{km\,s^{-1}}} \, M_\odot\,\mathrm{yr^{-1}}, \qquad (29)$$

where we normalized the CSM velocity by the highest-velocity Gaussian component in the spectra. This tremendous mass-loss rate is discussed in Section 6.
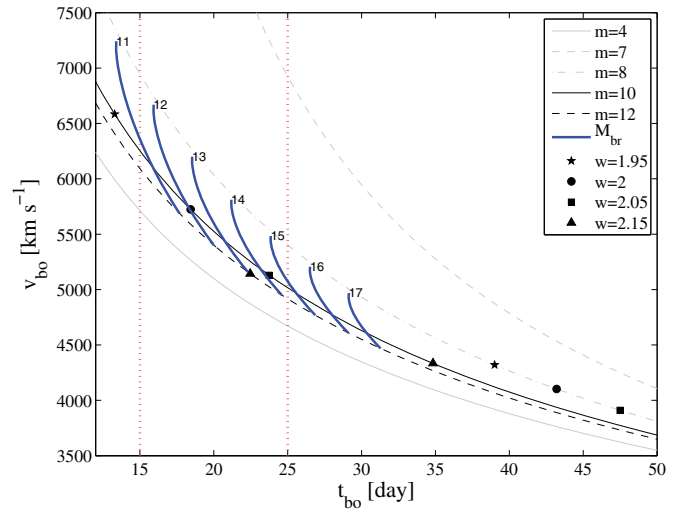
Figure 11 assumes $\epsilon = 1/4$. The reason for this choice is that it is expected that a shock propagating through the CSM will convert only the thermal energy stored in the ejecta to radiation. The thermal energy of the ejecta is roughly half of its kinetic energy (e.g., Nakar & Sari 2010). In addition, since the CSM is optically thick, at early times half the photons probably diffuse inward (and will be released at later times), therefore taking the efficiency roughly another factor of two down. However, at late times we expect the efficiency to increase to about $1/2$—therefore, ϵ may change slowly with time. Indication for this may be detected as a small deviation from the power-law decay in the first year (Figure 1). We note that the exact value of ϵ has a relatively small effect on the results. For example, assuming $\epsilon = 0.1$ ($\epsilon = 0.5$) gives $M_{\mathrm{br}} > 15\,M_\odot$ ($M_{\mathrm{br}} > 8\,M_\odot$).

Another assumption that goes into Figure 11 is that the bolometric correction in the first year is constant. However, as seen in Figures 1 and 4, there are some indications for variations in the bolometric correction. Given this uncertainty, we investigated the effect of variable bolometric correction on our results. Specifically, we assumed that the effective temperature of the photosphere evolves as $T = T_{\mathrm{bo}}(t/t_{\mathrm{bo}})^\beta$, where T_{bo} is the observed temperature at shock breakout (see Section 2). Assuming $T_{\mathrm{bo}} = 9000$ K and $t_{\mathrm{bo}} = 20$ day, we corrected our light curve according to the bolometric correction we get from the temperature, and we investigated the effect of β on our results. We find that for $-0.2 < \beta < 0.1$ the estimate on M_{br} does not change by more than 20%. Figures 3 and 4 suggest that $|\beta| \lesssim 0.1$. Another unknown factor is the opacity κ. Increasing κ to 0.5 cm^2 g^{-1} will set $M_{\mathrm{br}} \gtrsim 8\,M_\odot$.

The entire analysis presented here assumes that the CSM and ejecta have spherical symmetry. This is likely not the case (e.g., Patat et al. 2011). However, an order-of-unity deviation from spherical geometry will not change the results dramatically since the integrated luminosity depends on the total mass of the CSM.

Table 7
Derived SN and CSM Properties

t_{bo} (day)	m	L_0 (erg s^{-1})	α_1	w	K (g cm^{w-3})	r_{bo} (cm)	v_{bo} (km s^{-1})	M_{br} ($M_\odot$)
15	10	7.4×10^{45}	-0.36	. . .	. . .	. . .	. . .	. . .
	12			2.09	3.0×10^{18}	8.7×10^{14}	6100	9.8
20	**10**	1.2×10^{46}	-0.38	2.01	3.0×10^{17}	1.1×10^{15}	5500	12.8
	12			2.13	1.7×10^{19}	1.0×10^{15}	5400	12.0
25	10	1.8×10^{46}	-0.41	2.06	2.0×10^{18}	1.2×10^{15}	5000	14.8
	12			2.17	8.9×10^{19}	1.2×10^{15}	4900	14.2
30	10	2.7×10^{46}	-0.43	2.11	1.2×10^{19}	1.4×10^{15}	4600	16.9
	12			2.21	4.3×10^{20}	1.3×10^{15}	4600	16.4

Notes. The various parameters for different values of t_{bo} and m. The calculations assume $\epsilon = 1/4$ and $\kappa = 0.34$ cm^2 g^{-1}. The adopted values of t_{bo} and m are marked in boldface. Missing data indicate that $w < 2$ and therefore the solution is not valid (see text).

In order for the results (and specifically the M_{br} estimate) to change significantly, an extreme geometry is probably required. We cannot rule out such a scenario. However, given that our model explains the observed broken-power-law behavior, finds values of m and w that are consistent with expectations, and successfully predicts the observed shock velocity (see also Sections 5.2 and 5.3), we conclude that our description is correct. Another important point may be the clumpiness of the CSM. However, if the Chevalier (1982) solutions are still valid on average, our results are correct, as they depend on the global (average) properties of the CSM and ejecta. Therefore, we conclude that our main result that the mass in the CSM of SN 2010jl is in excess of about 10 $M_\odot$ is robust. Finally, we note that Svirski et al. (2012) predict that at early times the color temperature will evolve slowly with time. This is roughly consistent with the observations of SN 2010jl.

5.2. Late-time Light Curve

Around 300 days after maximum light, the optical light curve of SN 2010jl shows a break in its power-law evolution, and the R-band power-law index becomes $\alpha_2 \approx -3$. The change in power-law slope at late times may have three possible explanations: (1) we reached the snow-plow phase, and therefore m changes to about 4 (Svirski et al. 2012); (2) the shock became slow cooling and therefore the light curve drops rapidly; and (3) the shock reached the end of the CSM, or in other words, the CSM density profile became steeper than r^{-2}. Next, we will test these possibilities and find that the snow-plow phase option is the most likely. We note that the measurement of M_{br} is not affected by the nature of the break.

Our solution suggests that the CSM density at r_{br} is $\sim 10^9$ cm^{-3}. Given this very high density, the shock must be fast cooling and option (2) can be ruled out (Equation (15); see also Figure 12, panel (d)). Assuming $m = 10$, Equation (12) suggests that in order to get the observed value $\alpha_2 \approx -3$, we require $w \approx 5$. However, the Chevalier (1982) self-similar solutions are invalid for $w > 3$. Nevertheless, the steep value of α_2 probably means that if $m \approx 10$, $w > 3$. We note that in this case, the shock will accelerate, and at late times we expect $v_s \gtrsim 4000$ km s^{-1} (Figure 12). This is somewhat higher than the velocity suggested by our *NuSTAR* observations (see Section 5.3).

Given the solution presented in Figure 11 (using α_1), integration of the mass to the break radius gives $M_{br} \gtrsim 10 M_\odot$. Normal SN explosions have an ejecta mass that is similar, to an order of magnitude, to our derived CSM mass. Therefore, it is

likely that the ejecta collected a CSM mass that is equivalent to its own mass and the system reached the snow-plow phase, and hence there is a natural explanation to the change in α without changing w (at least not in a major way). Of course, it is possible that during t_{br} the values of both m and w are changing. This idea requires a coincidence between two independent phases, and therefore we will not discuss it further.

Assuming $w = 2$ and $m = 4$, we expect $\alpha_2 \approx -3/2$ (see also Svirski et al. 2012), while we observed $\alpha_2 \approx -3$. There are several possibilities to explain this. First, at late times (a year after peak brightness) there may be significant evolution in the bolometric correction. Interestingly, the late-time spectra (see Figure 2) suggest that the SN becomes bluer at late times. We note, however, that these late-time measurements are affected by the underlying star-forming region and are therefore uncertain. In addition, the missing radiation may be emitted in the X-ray band. We find that if the intrinsic unabsorbed X-ray luminosity of the SN is ~ 20 times higher than observed, the contribution of the X-ray luminosity to the bolometric light curve will modify α_2 to about $-3/2$.

A second possibility is that the system is approaching the slow cooling stage and some of the energy is not released efficiently as optical photons. Our estimate suggests that at late times the cooling timescale is increasing to about 10% of the dynamical timescale (Figure 12). Therefore, it is possible that the shock starts to be nonradiative, hence explaining the steeper than expected power-law slope. To summarize the issue, we suggest that the most likely explanation to the discrepancy between the observed and predicted value of α_2 is that at late times there is a substantial bolometric correction, and possibly the shock is becoming nonradiative. Unfortunately, we do not have reliable multi-band or spectroscopic observations during the second year.

Based on our simple model, Figure 12 shows the evolution of the various parameters as a function of time. Panel (b) indicates that even at late times, about 3 yr after maximum light, the density of the CSM at the shock radius is of order a few times 10^8 cm^{-3}. Interestingly, the Thomson optical depth above the shock, 3 yr after maximum light, is decreased to roughly unity. This may explain why the visible-light spectrum of the SN is becoming bluer, as the region heated by the shock is becoming more exposed and the photons emitted in the shock region are affected by less and less processing. The free–free optical depth [panel (f)] above the shock at 10 GHz, 3 yr after maximum light, is $\tau_{ff} \approx 10^5$, assuming that the electron temperature above the shock is 10^4 K. Therefore, naively, radio emission is not
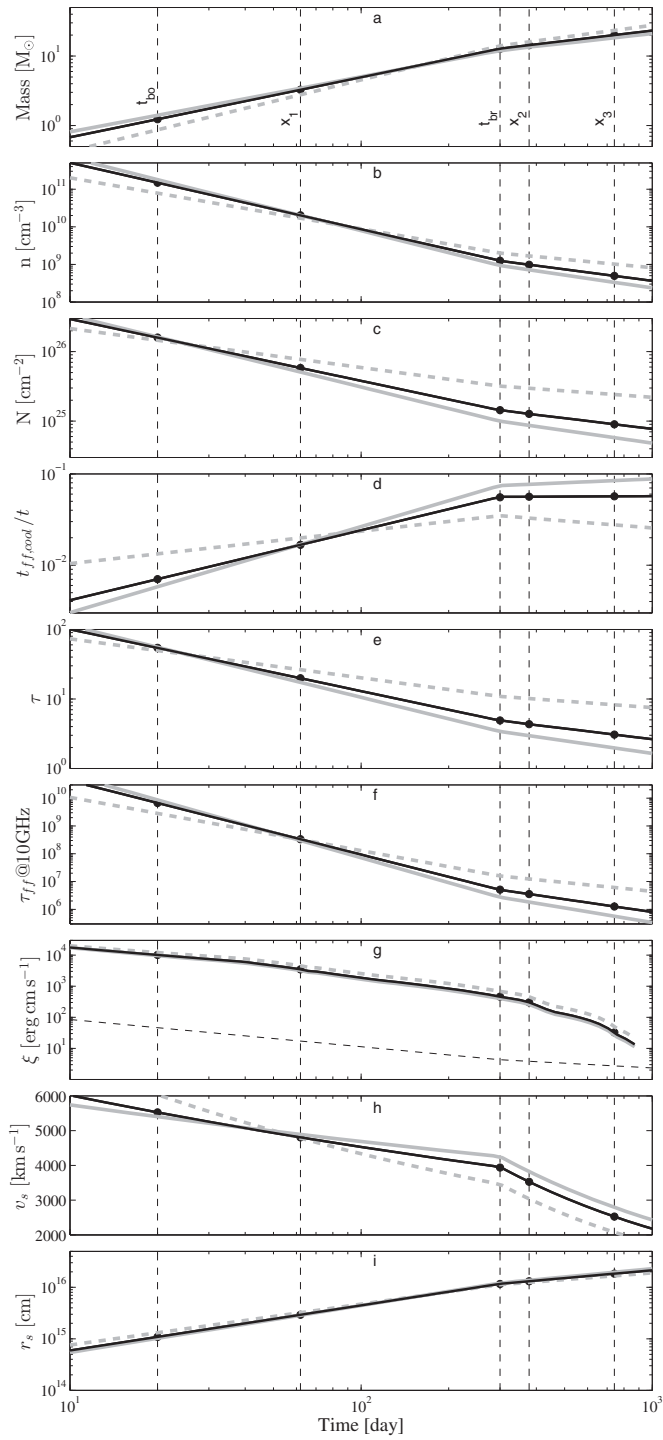
Figure 12. CSM properties as a function of time, assuming $t_{bo} = 20$ day and $m = 10$ (black lines). The gray lines are for $m = 12$, while the dashed-gray line is for $m = 8$. The black dashed vertical lines show the breakout timescale (t_{bo}), the time of the optical light-curve break (300 days; t_{br}), the times of the first two *Chandra* epochs (x_1 and x_2), and the *XMM* + *NuSTAR* epoch (x_3). The different panels show the following: (a) CSM mass within the shock radius, (b) density of the CSM at the shock radius, (c) column density between the shock and the observer, (d) free–free cooling timescale divided by the time at the shock radius, (e) Thomson optical depth between the shock radius and the observer, (f) 10 GHz free–free optical depth, (g) ionization parameter (Equation (28)), (h) shock velocity, and (i) shock-radius evolution. Time is measured relative to maximum *I*-band light minus t_{bo}. We note that panel (g) shows an additional dashed black line; it represents the minimal ionization parameter (for $m = 10$) as estimated by replacing the luminosity in Equation (28) by the observed X-ray luminosity ($L_X \approx 1.5 \times 10^{41}$ erg s^{-1}). The intrinsic X-ray luminosity may be much higher because of, for example, bound-free absorption.

expected in the near future. However, if the electron temperature just above the shock is significantly higher and the CSM cocoon is terminated at a few times the shock radius, then τ_{ff} can be small enough and radio emission would be detected. Finally, we note that the cooling timescale divided by the hydrodynamical timescale [panel (d)] suggests that at late times, the system may approach slow cooling, so some energy losses (not in optical radiation) are expected.

An interesting point to note is that Figures 3 and 4 show that at late times the effective blackbody radius is decreasing. Svirski et al. (2012) argue that at late times the fraction of the energy released in X-rays is increasing (as seen in SN 2010jl). In this case, the optical photons will deviate from a blackbody spectrum as fewer photons are available in the optical, and this can generate an apparent decrease in the effective blackbody radius. In general, this effect should caution against the use of blackbody fits to estimate the photospheric radius of such explosions.

5.3. Modeling the X-Ray Data

We still do not have a good theoretical understanding of the expected X-ray spectral evolution from optically thick sources (e.g., Katz et al. 2011; Chevalier & Irwin 2012; Svirski et al. 2012). Another problem is that the X-ray spectral observations are hard to model. The reasons are the low number of photons, contamination from nearby sources, and the degeneracy between the free parameters in the various models. Nevertheless, it is interesting to compare the rough expectations with the observations. Given these issues, our approach is to use the model we constructed based on the optical data to make some predictions for the X-ray band, and to compare the X-ray observations with these predictions. Especially interesting are the *NuSTAR* + *XMM* observations, which cover a large energy range and were taken when the Thomson optical depth is expected to be relatively low, $\tau \approx 3$. Here we discuss the bound-free absorption, the X-ray flux, and the X-ray spectrum.

Figure 12 shows that the predicted column density above the shock is very large, $\sim 10^{26}$ cm^{-2} during the shock breakout, dropping to $\sim 10^{25}$ cm^{-2} during our *XMM* + *NuSTAR* observations. These predicted column densities are larger, by about two orders of magnitude, than the bound-free column densities suggested by Chandra et al. (2012a) at early times. A plausible explanation is that the CSM above the shock is ionized by the SN radiation field. Indeed, panel (g) in Figure 12 suggests that at early times the ionization parameter (Equation (28)) is $>10^2$ erg cm s^{-1}, and possibly as high as $\sim 10^4$ erg cm s^{-1}. Such a large value is enough to ionize all the metals in the CSM (Chevalier & Irwin 2012). However, at late times, the ionization parameter is only $\sim 10^2$ erg cm s^{-1}, which may leave some bound electrons in heavy elements.

The next simple test is to use the order-of-magnitude estimate in Equation (27) to predict the X-ray flux as a function of time. The prediction is shown in Figure 6 as a gray line. At early times, about 100 days after the SN maximum visible light, the prediction is consistent with the observations. About a year later, the X-ray prediction is a factor of four higher than the observations, while around 2.5 yr after maximum visible light, the predicted X-ray luminosity is a factor of two higher than observed. We note that Equation (27) is an order-of-magnitude estimate of the luminosity in the entire X-ray band (including soft and hard (>10 keV) X-rays), and that it does not take into account the bound-free absorption, which, even if not very high, still can affect the emission of soft X-rays considerably.
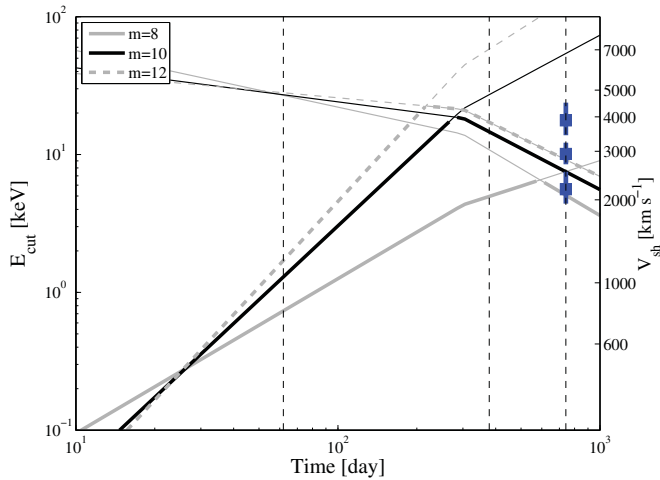
Figure 13. Predicted X-ray cutoff energy (Equation (26)) as a function of time. Different line types and gray-scale levels are for different values of m as indicated in the legend. The heavy lines represent the minimum function (Equation (26)), while the thin lines represent the two possibilities in Equation (26) without taking the minimum. The blue squares show the temperature as measured in the *NuSTAR + XMM* epoch (Table 6; faint sources removed). The upper square is for the zvphabs*mekal model, the bottom square refers to zvphabs*powerlaw*spexpcut, and the square in the middle is for zvphabs*powerlaw*spexpcut with $\Gamma = 1$. The vertical dashed lines show the epochs of the two *Chandra* and the *NuSTAR + XMM* observations. The right-hand ordinate axis gives the shock velocity corresponding to the cutoff energy, based on Equation (25).

(A color version of this figure is available in the online journal.)

For example, for $N_H = 10^{22}$ cm^{-2}, the bound-free optical depth (e.g., Morrison & McCammon 1983) at 0.5 keV (1 keV) is 7.3 (2.4), which will decrease the observed X-rays at this energy by a factor of 1600 (11).

According to Svirski et al. (2012), at early times we expect that the cutoff energy will be around $m_e c^2/\tau^2$, while when the optical depth decreases to roughly a few, we expect that the cutoff energy will represent the shock temperature (Equation (26)). Figure 13 shows the predicted cutoff energy as a function of time. Also plotted are the *NuSTAR + XMM* measured X-ray temperatures based on the various fits (Table 6) and assuming temperature equilibrium between the ions and the electrons. If equilibrium is not present, then our measurement is only a lower limit on the shock velocity.

Figure 13 suggests that the *NuSTAR + XMM* observation measures the shock temperature, and hence the shock velocity. The three models in Table 6 in which the faint nearby sources were removed suggest a shock velocity with 1σ confidence interval in the range 1900–4500 km s^{-1}. We suggest that the most physically motivated model is the power-law model with exponential cutoff, in which the power-law index is set to $\Gamma = 1$. The reason is that below the cutoff energy we speculate that free–free processes, with a spectrum $n(E) \propto E^{-1}$, will dominate the emission (Svirski et al. 2012). This model suggests an exponential cutoff energy $kT = 10.1^{+2.1}_{-1.6}$ keV, which translates to $v_s \approx 2900 \pm 300$ km s^{-1}. However, if the ions and the electrons are not in equilibrium, all we can say is that the shock velocity is larger than ~ 2000 km s^{-1}. This measured shock velocity is in agreement with the predicted shock velocity of ~ 2600 km s^{-1} (Figure 12, panel (h)). Under the assumption that the SN is powered by interaction, by comparing the kinetic energy to the integrated luminosity, the X-ray-derived velocity, along with the integrated bolometric luminosity, can be used to roughly determine the CSM mass. While lacking the exact

prefactors we derived in Section 4.2, we obtain an order-of-magnitude estimate of the CSM mass—$\sim 10 M_\odot$.

We estimate that during the *NuSTAR + XMM* observation the ionization parameter was $\sim 10^2$ erg cm s^{-1}. According to Chevalier & Irwin (2012), this value is not enough to ionize all of the metals. Therefore, our estimate of the ionization parameter is in conflict with the value of the bound-free column density we deduced from the *NuSTAR + XMM* observations. Possible solutions include the existence of even harder photons in the shock, or that the estimate of the effective ionization parameter at high optical depth is wrong.

Given the difficulties in modeling the early-time data obtained by *Chandra*, we attempt to fit these observations with a power law having an exponential cutoff as predicted by Equation (26) (Figure 13)—1.5 keV and 15 keV, for the *Chandra* first and second epochs, respectively. While the fit to the second epoch has an acceptable C-statistic (see Table 6), fitting the first epoch while freezing the cutoff energy at 1.5 keV failed. Given the unknowns associated with the X-ray emission at such high optical depth ($\tau \approx 20$), we do not consider this to be a problem for our model.

We note that the marginal detection of the Kα line in the first *Chandra* epoch (Section 3) is not naturally explained in our model. In the context of our model, the Kα line must be generated at relatively large radii where the optical depth is low.

5.4. Emission-line Spectra and Precursor

The spectra of SN 2010jl show a variety of emission lines. Based on spectropolarimetric observations, Patat et al. (2011) suggested that the Balmer lines form above the photosphere. Therefore, the emission from the Balmer lines will not constitute a good estimate of the mass in the CSM (see discussion in Ofek et al. 2013c). Smith et al. (2012) show that the line shape evolves with time, presumably due to the formation of dust.

Nevertheless, the width of the Balmer lines gives us an estimate of the CSM velocity. This is important in order to estimate when the CSM was ejected from the SN progenitor. Given the velocities of the Balmer lines of SN 2010jl (between ~ 70 km s^{-1} and ~ 300 km s^{-1}; Section 2.2), and the typical radii of the CSM of $\sim 2 \times 10^{16}$ cm, we estimate that the CSM was ejected from the progenitor ~ 10–100 yr prior to the explosion. Given this prediction, we searched for archival images at this sky location. PTF images of the SN location taken about 200 days prior to explosion did not reveal any pre-explosion outburst; see E. O. Ofek et al. (in preparation) for details.

6. SUMMARY AND DISCUSSION

We present optical and X-ray observations of SN 2010jl (PTF 10aaxf). We extend the model described by Svirski et al. (2012) for an SN shock interacting with an optically thick CSM. Our model treats many of the unknowns in the problem as free parameters. We show that this model explains many of the details in the optical and X-ray data. Most interestingly, using this model we find that the mass in the CSM must be larger than $\sim 10 M_\odot$, and possibly smaller than $16 M_\odot$. This large amount of mass must have been ejected from the SN progenitor several decades prior to its explosion. We note that preliminary results based on the radiation hydrodynamics light-curve code described by Frey et al. (2013) support our results regarding the large CSM mass required to power SN 2010jl (W. Even et al., in preparation).

Our model demonstrates that the optical light curves of SNe IIn driven by interaction of the SN ejecta with optically thick CSM are characterized by long-lived power laws. Furthermore, the optical light curves can be used in a straightforward way to measure the properties of the CSM, as well as the SN shock velocity and its evolution with time. We note that the shock velocity is directly related to the energetics of the explosion. We argue that measurements of the shock velocity based on spectral line widths are likely not as accurate as this method, since they depend on where the spectral lines are forming. We note that a similar model, but such that neglects the snowplow phase, has been recently suggested by Moriya et al. (2013).

SN 2010jl is the first SN to be detected in the hard X-ray band using *NuSTAR*. The *NuSTAR* observation combined with *XMM* data taken roughly at the same time enable us to measure the temperature of this emission. From our model, we show that this temperature likely represents the shock velocity, and that the measured shock velocity of $\sim$3000 km s^{-1} is consistent with the prediction of our model, based on the optical data alone. This demonstrates the power of hard X-ray observations to measure the SN shock velocity, and possibly even the evolution of the shock velocity with time.

Interestingly, our modeling prefers solutions with CSM density profiles $\propto r^{-2}$ (i.e., wind-like profile). This means that either the CSM was ejected in a continuous process, or multiple bursts, or in a concentrated burst with a *velocity* distribution having a power-law index of $\sim$2, and in which the ratio between the velocity of the fast and slowly moving ejecta is at least a factor of 20. This factor is required in order to explain the shock emission that was probed from a distance of $\sim$10^{15} cm up to more than $\sim$2 $\times$ 10^{16} cm.

Several mechanisms have been suggested to explain the presence of large amounts of CSM around SN progenitors. Quataert & Shiode (2012) and Shiode & Quataert (2013) propose that dissipation of gravity waves originating from the stellar core can unbind large amounts of mass. Chevalier (2012) suggests that a common-envelope phase just prior to explosion may be responsible for the CSM. Soker & Kashi (2013) argue for outbursts driven by binary star periastron passages, and Arnett & Meakin (2011) show that shell oxygen burning in massive stars gives rise to large fluctuations in the turbulent kinetic energy that in turn may produce bursts. The most thoroughly explored mechanism is probably the pulsational pair instability (Rakavy et al. 1967; Woosley et al. 2007; Waldman 2008), which predicts that some massive stars will eject material several times before their final and last explosion. Given the large amount of CSM involved, it is possible that SN 2010jl is a result of multiple pulsational pair instabilities taking place over the past several decades. Multiple mass ejection events are required in order to explain the average r^{-2} CSM radial distribution over a factor of 20 in radii. However, other explanations may exist (e.g., Quataert & Shiode 2012; Chevalier 2012).

REFERENCES

Arnaud, K. A. 1996, in ASP Conf. Ser. 101, Astronomical Data Analysis Software and Systems V, ed. G. H. Jacoby & J. Barnes (San Francisco, CA: ASP), 17
Arnett, W. D., & Meakin, C. 2011, ApJ, 741, 33
Balberg, S., & Loeb, A. 2011, MNRAS, 414, 1715
Benetti, S., Bufano, F., Vinko, J., et al. 2010, CBET, 2536, 1
Brown, P. J., Holland, S. T., Immler, S., et al. 2009, AJ, 137, 4517
Burrows, D. N., Hill, J. E., Nousek, J. A., et al. 2005, SSRv, 120, 165
Cardelli, J. A., Clayton, G. C., & Mathis, J. S. 1989, ApJ, 345, 245
Chandra, P., Chevalier, R. A., Chugai, N., et al. 2012a, ApJ, 755, 110
Chandra, P., Chevalier, R. A., Irwin, C. M., et al. 2012b, ApJL, 750, L2
Chevalier, R. A. 1982, ApJ, 259, 302
Chevalier, R. A. 1998, ApJ, 499, 810
Chevalier, R. A. 2012, ApJL, 752, L2
Chevalier, R. A. 2013, in IAU Symp. 296, Supernova Environmental Impacts, ed. A. Ray & R. McCray (Cambridge: Cambridge Univ. Press)
Chevalier, R. A., & Fransson, C. 1994, ApJ, 420, 268
Chevalier, R. A., & Irwin, C. M. 2011, ApJL, 729, L6
Chevalier, R. A., & Irwin, C. M. 2012, ApJL, 747, L17
Chugai, N. N., Cumming, R. J., Blinnikov, S. I., et al. 2003, arXiv:astro-ph/0309226
Chugai, N. N., & Danziger, I. J. 1994, MNRAS, 268, 173
Corsi, A., Ofek, E. O., Gal-Yam, A., et al. 2013, arXiv:1307.2366
Dickey, J. M., & Lockman, F. J. 1990, ARA&A, 28, 215
Dopita, M. A., Cohen, M., Schwartz, R. D., & Evans, R. 1984, ApJL, 287, L69
Draine, B. T., & McKee, C. F. 1993, ARA&A, 31, 373
Efron, B. 1982, The Jackknife, the Bootstrap and Other Resampling Plans (Philadelphia, PA: Society for Industrial and Applied Mathematics)
Efron, B., & Tibshirani, R. J. 1993, An Introduction to the Bootstrap, Monographs on Statistics and Applied Probability 57 (London: Chapman and Hall/CRC)
Falk, S. W., & Arnett, W. D. 1973, ApJL, 180, L65
Falk, S. W., & Arnett, W. D. 1977, ApJS, 33, 515
Filippenko, A. V. 1997, ARA&A, 35, 309
Foley, R. J., Berger, E., Fox, O., et al. 2011, ApJ, 732, 32
Foley, R. J., Smith, N., Ganeshalingam, M., et al. 2007, ApJL, 657, L105
Fraser, M., Magee, M., Kotak, R., et al. 2013, ApJL, 779, L8
Frey, L. H., Even, W., Whalen, D. J., et al. 2013, ApJS, 204, 16
Gal-Yam, A. 2012, Sci, 337, 927
Gal-Yam, A., & Leonard, D. C. 2009, Natur, 458, 865
Gal-Yam, A., Leonard, D. C., Fox, D. B., et al. 2007, ApJ, 656, 372
Gehrels, N., Chincarini, G., Giommi, P., et al. 2004, ApJ, 611, 1005
Ghavamian, P., Schwartz, S. J., Mitchell, J., Masters, A., & Laming, J. M. 2013, SSRv, 178, 633

Ginzburg, S., & Balberg, S. 2012, ApJ, 757, 178
Gnat, O., & Sternberg, A. 2009, ApJ, 693, 1514
Harrison, F. A., Craig, W. W., Christensen, F. E., et al. 2013, ApJ, 770, 103
Itoh, H. 1978, PASJ, 30, 489
Kasen, D., & Bildsten, L. 2010, ApJ, 717, 245
Katz, B., Sapir, N., & Waxman, E. 2011, arXiv:1106.1898
Kiewe, M., Gal-Yam, A., Arcavi, I., et al. 2012, ApJ, 744, 10
Lang, K. R. 1999, Astrophysical Formulae (New York: Springer)
Law, N. M., Kulkarni, S. R., Dekany, R. G., et al. 2009, PASP, 121, 1395
Matzner, C. D., & McKee, C. F. 1999, ApJ, 510, 379
Mauerhan, J. C., Smith, N., Filippenko, A., et al. 2013, MNRAS, 430, 1801
Mewe, R., Lemen, J. R., & van den Oord, G. H. J. 1986, A&AS, 65, 511
Moretti, A., Campana, S., Tagliaferri, G., et al. 2004, Proc. SPIE, 5165, 232
Moriya, T. J., Maeda, K., Taddia, F., et al. 2013, MNRAS, 435, 1520
Moriya, T. J., & Tominaga, N. 2012, ApJ, 747, 118
Morrison, R., & McCammon, D. 1983, ApJ, 270, 119
Murase, K., Thompson, T. A., Lacki, B. C., & Beacom, J. F. 2011, PhRvD, 84, 043003
Murase, K., Thompson, T. A., & Ofek, E. O. 2013, arXiv:1311.6778
Nakar, E., & Sari, R. 2010, ApJ, 725, 904
Newton, J., & Puckett, T. 2010, CBET, 2532, 1
Nomoto, K., & Sugimoto, D. 1972, PThPh, 48, 46
Nugent, P. E., Sullivan, M., Cenko, S. B., et al. 2011, Natur, 480, 344
Ofek, E. O., Cameron, P. B., Kasliwal, M. M., et al. 2007, ApJL, 659, L13
Ofek, E. O., Fox, D., Cenko, S. B., et al. 2013a, ApJ, 763, 42
Ofek, E. O., Laher, R., Law, N., et al. 2012a, PASP, 124, 62
Ofek, E. O., Laher, R., Surace, J., et al. 2012b, PASP, 124, 854
Ofek, E. O., Lin, L., Kouveliotou, C., et al. 2013b, ApJ, 768, 47
Ofek, E. O., Rabinak, I., Neill, J. D., et al. 2010, ApJ, 724, 1396
Ofek, E. O., Sullivan, M., Cenko, S. B., et al. 2013c, Natur, 494, 65
Pastorello, A., Cappellaro, E., Inserra, C., et al. 2013, ApJ, 767, 1
Pastorello, A., Smartt, S. J., Mattila, S., et al. 2007, Natur, 447, 829
Patat, F., Taubenberger, S., Benetti, S., Pastorello, A., & Harutyunyan, A. 2011, A&A, 527, L6
Poole, T. S., Breeveld, A. A., Page, M. J., et al. 2008, MNRAS, 383, 627
Quataert, E., & Shiode, J. 2012, MNRAS, 423, L92
Quimby, R. M., Kulkarni, S. R., Kasliwal, M. M., et al. 2011, Natur, 474, 487
Rakavy, G., Shaviv, G., & Zinamon, Z. 1967, ApJ, 150, 131
Rau, A., Kulkarni, S. R., Law, N. M., et al. 2009, PASP, 121, 1334
Rest, A., Foley, R. J., Gezari, S., et al. 2011, ApJ, 729, 88
Roming, P. W. A., Kennedy, T. E., Mason, K. O., et al. 2005, SSRv, 120, 95
Schafer, R. A. 1991, XSPEC, an X-ray Spectral Fitting Package: Version 2 of the User's Guide (Paris, France: European Space Agency)
Schlegel, D. J., Finkbeiner, D. P., & Davis, M. 1998, ApJ, 500, 525
Shiode, J. H., & Quataert, E. 2013, arXiv:1308.5978
Slysh, V. I. 1990, SvAL, 16, 339
Smith, N., Chornock, R., Li, W., et al. 2008, ApJ, 686, 467
Smith, N., Li, W., Foley, R. J., et al. 2007, ApJ, 666, 1116
Smith, N., Miller, A., Li, W., et al. 2010, AJ, 139, 1451
Smith, N., Silverman, J. M., Chornock, R., et al. 2009, ApJ, 695, 1334
Smith, N., Silverman, J. M., Filippenko, A. V., et al. 2012, AJ, 143, 17
Soker, N., & Kashi, A. 2013, ApJL, 764, L6
Stoll, R., Prieto, J. L., Stanek, K. Z., et al. 2011, ApJ, 730, 34
Svirski, G., Nakar, E., & Sari, R. 2012, ApJ, 759, 108
Waldman, R. 2008, ApJ, 685, 1103
Waxman, E., & Shvarts, D. 1993, PhFl, 5, 1035
Weaver, T. A. 1976, ApJS, 32, 233
Weiler, K. W., Van Dyk, S. D., Discenna, J. L., Panagia, N., & Sramek, R. A. 1991, ApJ, 380, 161
Woosley, S. E., Blinnikov, S., & Heger, A. 2007, Natur, 450, 390
Yamanaka, M., Okushima, T., Arai, A., Sasada, M., & Sato, H. 2010, CBET, 2539, 1
Yaron, O., & Gal-Yam, A. 2012, PASP, 124, 668
Zhang, T., Wang, X., Wu, C., et al. 2012, AJ, 144, 131